Session 1P5
Modelling, Imaging and Inversion of Large-Scale Electromagnetic Data

On the Low-frequency Modeling of Coupled Obstacles Buried in Earth-like Medium

A. Breard (CNRS-SUPÉLEC-UPS, France); G. Perrusson (CNRS-SUPÉLEC-UPS, France); D. Lesselier (CNRS-SUPÉLEC-UPS, France); 372

NSA Calculation of Anechoic Chamber Using Method of Moment

T. Sasaki (Musashi Institute of Technology, Japan); Y. Watanabe (Musashi Institute of Technology, Japan); M. Tokuda (Musashi Institute of Technology, Japan); 373

Optimal Grids for the Forward and Inverse Electric Impedance Tomography Problems

F. Guevara Vasquez (Rice University, USA); L. Borcea (Rice University, USA); V. Druskin (Schlumberger-Doll Research, USA); 379

Finite-difference Solution of the 3D EM Problem Using Integral Equation Type Preconditioners

M. Zaslavsky (Schlumberger-Doll Research, USA); S. Davydycheva (Schlumberger-Doll Research, USA); V. Druskin (Schlumberger-Doll Research, USA); L. Knizhnerman (Schlumberger-Doll Research, USA); A. Abubakar (Schlumberger-Doll Research, USA); T. M. Habashy (Schlumberger-Doll Research, USA); . 380

An Effective Inversion Method Based on the Padé via Lanczos Process

R. F. Remis (Delft University of Technology, The Netherlands); 381

Inversion of Large-scale Electromagnetic Data through the Iterative Multizooming Reconstruction of Non-measurable Equivalent Current Densities

M. Donelli (University of Trento, Italy); D. Franceschini (University of Trento, Italy); M. Benedetti (University of Trento, Italy); A. Massa (University of Trento, Italy); G. L. Gragnani (University of Genoa, Italy); 385

QN Inversion of Large-scale MT Data

A. D. Avdeeva (Dublin Institute for Advanced Studies, Ireland); D. B. Avdeev (IZMIRAN, Russian Academy of Sciences, Russia); 386

2.5D Algorithm for Tomographic Imaging of the Deep Electromagnetic Geophysical Measurement

A. Abubakar (Schlumberger, USA); T. M. Habashy (Schlumberger, USA); V. Druskin (Schlumberger, USA); D. Alumbaugh (Schlumberger, USA); P. Zhang (Schlumberger, USA); M. Wilt (Schlumberger, USA); L. Knizhnerman (Schlumberger, USA); 390

A Rigorous 3-D MT Inversion

D. B. Avdeev (Dublin Institute for Advanced Studies, Ireland); A. D. Avdeeva (Russian Academy of Sciences, Russia); 395

Contrast Source Inversion of 3D Electromagnetic Data

P. M. van den Berg (Delft University of Technology, The Netherlands); A. Abubakar (Schlumberger-Doll Research, USA); T. M. Habashy (Schlumberger-Doll Research, USA); 399

On the Low-frequency Modeling of Coupled Obstacles Buried in Earth-like Medium

A. Breard, **G. Perrusson**, **and D. Lesselier**
CNRS-SUPÉLEC-UPS, France

The work considered here focuses onto the characterization of homogeneous volumetric obstacles buried in a Earth-like homogeneous or half-space medium in the induction regime. Fields of application are in the magnetic probing of natural or artificial objects buried in subsoil at some distance from the air/soil interface.

By characterization, it is meant identification of number, locations and main electrical and geo- metrical features of these obstacles. The latter are assumed to be penetrable with somewhat higher conductivity than the one of the embedding medium (more resistive cases are also worthwhile). A typical obstacle geometry is the versatile yet simple ellipsoidal one and degenerate shapes. Usually one could assume two (or a small number of) such obstacles with different semi-axes and conductivities, somewhat close (in terms of the skin depth) to one another and lying in the near-field of a (vertical) magnetic dipole or a (horizontal) electrical current loop (the source), the magnetic field induced by the electromagnetic interaction being collected nearby at several locations along a borehole (within the Earth) or on a planar surface (above the Earth interface) and possibly at several frequencies variations of impedance of coil receivers could be considered as well.

The first step is to put together a proper modeling tool of the interaction. One is considering, inspired in that matter by earlier work for a single obstacle, G. Perrusson *et al*. Conductive masses in a half-space Earth in the diffusive regime: Fast hybrid modeling of a low-contrast ellipsoid, *IEEE Trans. Geosci. Remote Sens.* **38** 1585-1599 (2000), the extended Born approximation allied to traditional low-frequency asymptotics fields and all pertinent quantities are expanded in positive integer powers of (jk), k complex wavenumber of the exterior medium.

Thus, one is able to express the secondary electrical currents within the obstacles as volume integrals of products of source-independent depolarization tensors times primary fields, the coefficients up to power 3 in (jk) of the said tensors being expressed in closed-form for ellipsoidal shapes in their eigen co-ordinate systems, the coefficients of the primary fields being known or having been derived lately as well up to pertinent orders in both homogeneous and half-space cases for the sources indicated above.

Then, further simplification comes from the fact that, when the obstacles are small enough, the quantities which matter are the tensor coefficients at their centers times their volumes. Since the electrical excitation field at the center of one given obstacle appears as the sum of the primary field and the field due to all other obstacles, one easily arrives at a set of linear equations which yield the total electrical currents at every center (with closed-form solution for two obstacles); the magnetic fields they radiate or (via reciprocity) variations of probe impedances follow. Since all quantities are expanded into powers of (jk) coefficients of the series expansions are obtained in practice. Notice that one has to carefully book-keep all needed changes of coordinate systems from an absolute one to those of the ellipsoidal obstacles.

In this contribution, one will show how the machinery (a version of Lax-Foldy theory of multiple scattering, refer, e.g., to H. Braunisch, Methods in Wave Propagation and Scattering, PhD Thesis, MIT (2001), for a pure magneto-quasistatic development), can be worked out and how numerical results it provides compare with those from brute-force approaches and other approximations in various configurations. Time permitting, and depending upon the pace of the present investigation, retrievals of those obstacles using a differential evolution method will be considered briefly.

NSA Calculation of Anechoic Chamber Using Method of Moment

T. Sasaki, Y. Watanabe, and M. Tokuda
Musashi Institute of Technology, Japan

Abstract—NSA characteristics of an anechoic chamber were calculated by using the MoM (Method of Moment), and they were compared with those calculated by the FDTD method as well as the measured results in fully anechoic chamber. Next, we calculated of an anechoic chamber with complicated shapes. We found that first imitating a wave absorber using wire meshes with a limited electric conductivity is effective by controlling the wire interval. The NSA characteristics calculated by the MoM are as well as those calculated by the FDTD method. The NSA characteristics calculated by the MoM also agree with the measured results. And NSA characteristics of an anechoic chamber with complicated shapes were able to be calculated by using the MoM. Based on the results, it is confirmed that the MoM can be used to calculate NSA characteristics for an anechoic chamber.

1. Introduction

An anechoic chamber is a test room specially designed for completely shielding out external disturbances and for suppressing the echo caused by internal electromagnetic waves. The anechoic chamber for the radiated emission measurement specified by CISPR is usually evaluated by NSA (normalized site attenuation), which is a measure of the transmission characteristics between the standard antennas set inside the anechoic chamber. NSA is usually analyzed by using the ray tracing method [1], but the analytical accuracy of the NSA deteriorates in the low frequency band below several hundreds MHz because the ray tracing method approximates an electromagnetic wave as an optical ray. However, the FDTD (finite difference time domain) method is an analytical method that treats electromagnetic waves purely as waves. Therefore, the FDTD method can analyze NSA characteristics in the low frequency band below several hundreds MHz. The NSA of the anechoic chamber using the FDTD method was obtained by Holloway [2] and Takiguchi [3].

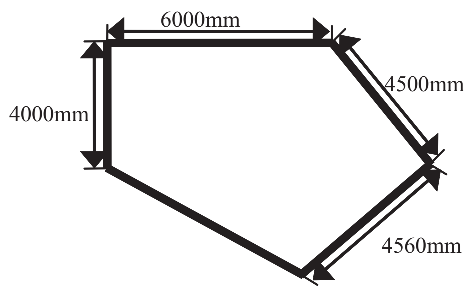

Figure 1: Anechoic chamber of analysis schedule.

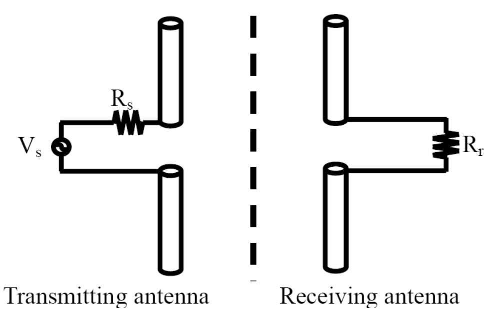

Figure 2: Modeling of transmitting and receiving antennas.

The purpose of this research is to construct and calculate an anechoic chamber that can measure below 30 MHz because we will measure the characteristics of a PLC (power line communication) system that operates between 2 to 30 MHz. Therefore the ray tracing method is not suitable for this calculation. The FDTD method is suitable, but it cannot be used to calculate the NSA of an anechoic chamber with a cross section of a non-rectangular shape, as shown in Figure 1. The non-rectangular shape is preferable because internal resonance of an anechoic chamber with such a cross section is lower than one with a rectangular cross section. Another way to calculate for the fully electromagnetic wave method is MoM (method of moment), which can calculate the NSA of an anechoic chamber with a non-rectangular cross section.

In this paper, we report on our comparison of calculations of the NSA of an anechoic chamber using the MoM and the FDTD method. In addition, we report on calculations of the NSA of an anechoic chamber with complicated shapes (pentagonal anechoic chamber) using the MoM. First, the NSA calculation of the antenna factor of transmitting and receiving antennas is presented. Second, we describe the modeling method of the anechoic chamber when we calculate the NSA characteristics using MoM. Third, we describe calculation results of NSA characteristics of the anechoic chamber is provided. Fourth, the calculation results obtained by the MoM are compared with those obtained by the FDTD method. Almost the same results were obtained. Finally, we calculated Characteristics of pentagonal anechoic chamber and showed that NSA characteristics of the pentagonal anechoic chamber are better than cuboid anechoic chamber.

2. Antenna Factor

Both transmitting and receiving antennas are set in the chamber to measure the NSA characteristics and then a modeling of antenna is required in a simulation. A half-wave dipole antenna was used by Takiguchi [3] for measuring the NSA characteristics of the anechoic chamber as transmitting and receiving antennas. Therefore, we have to model the half-wave dipole antenna by using the MoM. The modeled antennas are shown in Figure 2. In Figure 2, we modeled the transmitting antenna by putting the transmitting voltage (V_s) and the resistance (R_s) in a gap between two elements of the antenna. In Takiguchi's study [3], V_s was 1 V, and both R_s and R_r were 50 Ω, and the diameter of an antenna element was 7 mm.

Next, we examined the antenna factor modeling of a half-wave dipole antenna. The antenna factor AF represents the ratio of the electric field (abbreviated E-field) of an incident electromagnetic wave arriving at an antenna to the voltage induced by the incident wave between the antenna elements, as shown in (1).

$$AF = 20\log_{10}\left(\frac{E_0}{V_r}\right) \tag{1}$$

Where E_0 is the E-field strength at the antenna, and V_r is the induced voltage of the antenna. The E-field strength distribution near the antenna needs to be uniform when measuring the antenna factor. It is examined how many distances between the transmitting and receiving antennas is needed when calculating the antenna factor by using the MoM. Because the E-field strength at the receiving antenna does not depend on the frequency, we calculated the dependence of the E-field strength on the distance between the transmitting and receiving antennas at a frequency of 30 MHz as shown in Figure 3. In Figure 3, the difference in the E-field strength is negligible beyond 400 m. Therefore, we set the distance between the transmitting and the receiving antennas to 1 km.

A comparison of the calculation results of the antenna factor using the MoM with the antenna factor from Takiguchi's study is shown in Figure 4 [3], and their antenna factors clearly agree and have sufficient accuracy. Therefore, we used these calculated values.

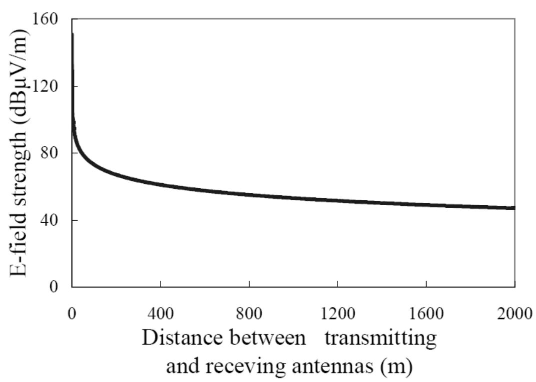

Figure 3: Dependence of E-field strength on the distance between transmitting and receving antennas.

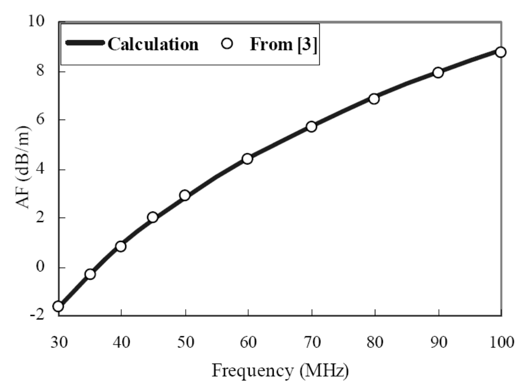

Figure 4: Calculation results of antenna factor by using MoM.

3. Modeling of Anechoic Chamber Using MoM

3.1. Modeling of Anechoic Chamber's Walls

The anechoic chamber had electromagnetic wave absorbers set on the walls and ceiling to suppress internal echo within the chamber. Two kinds of anechoic chamber were used, fully anechoic and semi anechoic.

In the fully anechoic chamber, all of the walls, the ceiling, and the floor are covered by wave absorbers, as depicted in Figure 5 However, in the semi anechoic chamber, the walls and ceiling are covered with the wave absorbers, but the floor is covered metal plates instead. Therefore, we had to imitate the wave absorbers to calculate the NSA characteristics for these anechoic chambers. We used a wire mesh with limited electric conductivity to imitate the wave absorbers for this study, as shown in Figure 6.

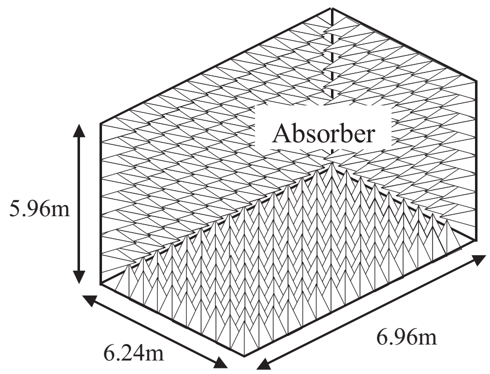

Figure 5: Construction of fully anechoic chamber.

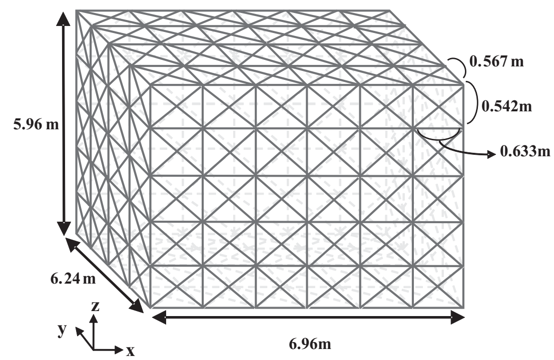

Figure 6: Modeling of fully anechoic chamber using MoM.

We chose the anechoic chamber used by Takiguchi [3] as a calculation object. The dimensions of the chamber are $W = 6.24\,\mathrm{m}$, $L = 6.96\,\mathrm{m}$ and $H = 5.96\,\mathrm{m}$. The walls, ceiling, and floor are composed of wire meshes with intervals of $W = 0.567\,\mathrm{m}$, $L = 0.633\,\mathrm{m}$, and $H = 0.542\,\mathrm{m}$, as shown in Figure 6, and the wire meshes also have diagonal wires. The interval of the wire meshes was a bit large comparing with the wavelength of the electromagnetic wave sent from the transmitting antenna to the receiving one. It should be small at a higher frequency, especially around 100 MHz, which was the highest frequency for this calculation. To make segment length $\lambda/10$ or less, the number of segments set here is 8706 in fully anechoic chamber and 7202 in semi anechoic chamber. The calculation model of the fully anechoic chamber is shown in Figure 6, but in the one for the semi anechoic chamber, the floor is modeled using a perfect ground.

3.2. Modeling of the Wave Absorber Reflection

The wave absorber imitates the wire mesh with a limited electric conductivity, which was calculated from the wave absorber's reflection coefficient. In this paper, we made reflecting plate and calculated reflection wave to transmission wave using MoM and obtained the limited electric conductivity corresponding to the amount of reflection. Figure 7 shows the calculation model of reflection. We set the distance between the transmitting antenna and the reflecting plate to 1 km. The reflection level is controlled by changing limited electric conductivity. The calculation method of the reflection is used space standing wave method [4]. This method is calculated from maximum and minimum electrical field strength (E_{max}, E_{min}), as shown in (2)

$$|\dot{\Gamma}| = \frac{1-\rho}{1+\rho} \quad \rho = \frac{E_{max}}{E_{min}} \tag{2}$$

where Γ is reflection coefficient, and ρ is standing wave ratio. In (2), ρ was adjusted by changing limited electric conductivity, and Γ was set as well as wave absorber's reflection by changing ρ. From here onwards, wave absorber was imitated by wire mesh with limited electric conductivity corresponding to wave absorber's reflection. In this paper, we calculated limited electric conductivity corresponding to reflection from 30 MHz to 100 MHz.

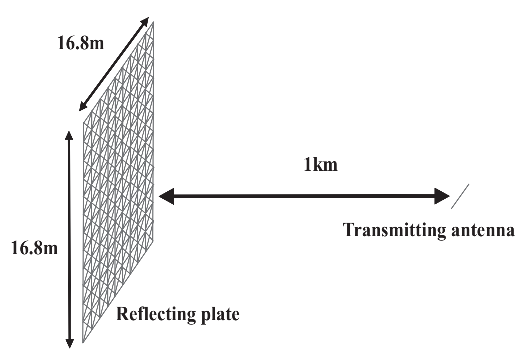

Figure 7: Calculated model of reflection.

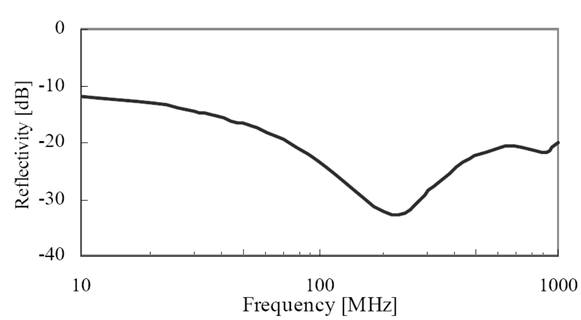

Figure 8: Reflectivity of wave absorber.

3.3. Reflectivity of the Wave Absorber

Figure 8 shows the reflectivity of the wave absorber measured by the rectangular coaxial air-line method. The reflectivity of the wave absorber is 20 dB above 70 MHz and reaches 30 dB near 200 MHz. For this calculation (30 to 100 MHz), it is supposed that a pyramidal foamed ferrite is not effective. But we have only the characteristics of synthesis of pyramidal foamed ferrite and ferrite tile. Therefore, we calculated using this characteristic.

4. NSA Calculation of Anechoic Chamber

4.1. Calculation Method of NSA

NSA represents the transmission characteristics between the transmitting and receiving antennas on the test site, and it is calculated by (3) [3]

$$NSA = V_{DIRECT} - V_{SITE} - (AF_T + AF_R) - \Delta NSA \ (dB) \tag{3}$$

where V_{DIRECT} is the received voltage of the measuring receiver when the connecting cables for a signal generator and the receiver are connected directly and V_{SITE} is the maximum receiving voltage of the measuring receiver when the cables are connected to the transmitting and receiving antennas and when the receiving antenna is swept between 1 and 4 m. AF_T and AF_R are the antenna factor of the transmitting and receiving antennas. ΔNSA is the correction value by direct coupling between the antennas, including image coupling between them through the metal ground plane. In this calculation, we used a half-wave dipole antenna at 30 MHz because this kind of dipole antenna was used in calculating the NSA with the FDTD method [3], and our intention is to compare the MoM and the FDTD method. In using MoM, Vsite are measured at 5points as shown Figure 9 and fully anechoic chamber, ΔNSA is zero [3].

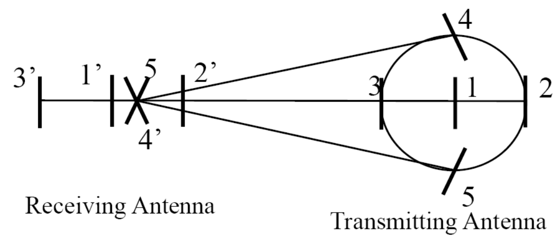

Figure 9: Position of transmitting and receiving antennas.

4.2. NSA Characteristics for Fully Anechoic Chamber

Figure 10 shows the calculation results for the NSA characteristics in the fully anechoic chamber where the MoM is used, and (a) is the vertical polarization, and (b) is the horizontal one. Curves from 1-1' to 5-5' are the calculation results using MoM for antenna position as shown Figure 10. In addition, the calculation results using the FDTD method and the measured results obtained from Takiguchi's study [3] are shown in Figure 10. The NSA characteristics calculated by the MoM in the frequency range from 30 to 100 MHz is similar to the measured results. The NSA calculation results using MoM hardly depend on various antenna positions. Especially, NSAs for 2-2' and 3-3' reached almost the same value as well as NSAs for 4-4' and 5-5'. However, the calculated NSA using the FDTD method does not agree with that using MoM. But, it is thought that the calculation accuracy using MoM is better than that using FDTD, because the humps existing the measured value is also appeared in NSA using MoM as shown Figure 10(a). NSA using MoM from 30 MHz to 60 MHz is fitted to the measured value more than NSA using FDTD. As the results, it is clear that the NSA characteristics calculated by using the MoM is more accurate than that calculated by using the FDTD method.

4.3. NSA Characteristics for Semi Anechoic Chamber

We also calculated the NSA characteristics of the semi anechoic chamber as shown in Figure 11. In Figure 11, (a) shows the vertical polarization, and (b) shows the horizontal polarization. In addition, for the semi anechoic chamber, the ΔNSA from the VCCI [5] was used. The NSA characteristics calculated by using the MoM for the semi anechoic chamber agree with the measured results. The difference among the calculation results using MoM for various antenna positions was not so many. The measured results of the NSA characteristics in the semi anechoic chamber have humps, and the calculated results using the MoM also appeared though it was not plenitude. Regardless, it is clear that the NSA characteristics calculated by using the MoM agrees with the measured results.

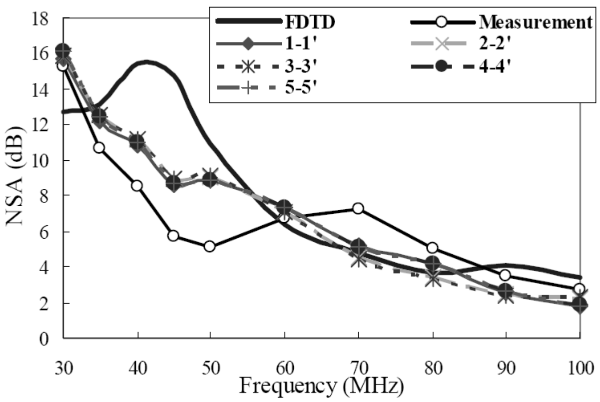

(a) Vertical polarization

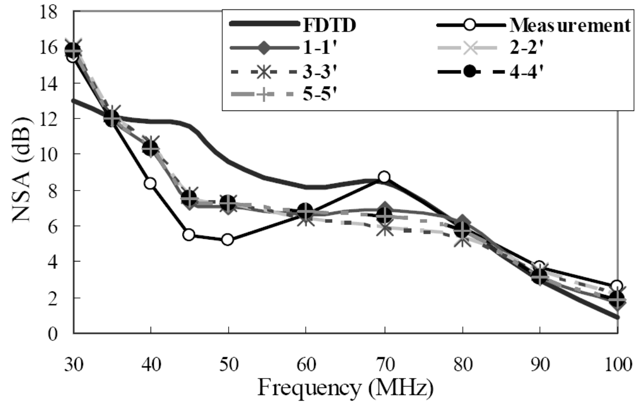

(b) Horizontal polarization

Figure 10: NSA characteristics of the fully anechoic chamber.

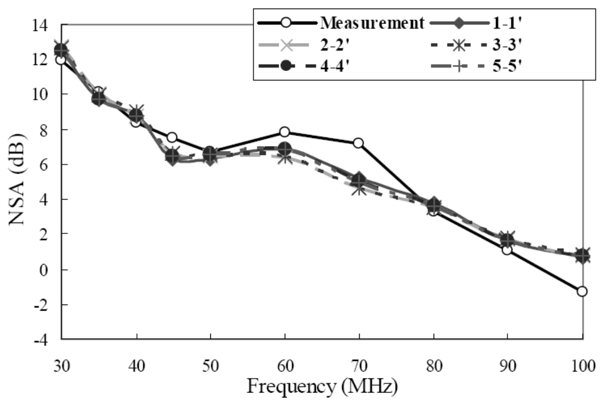

(a) Vertical polarization

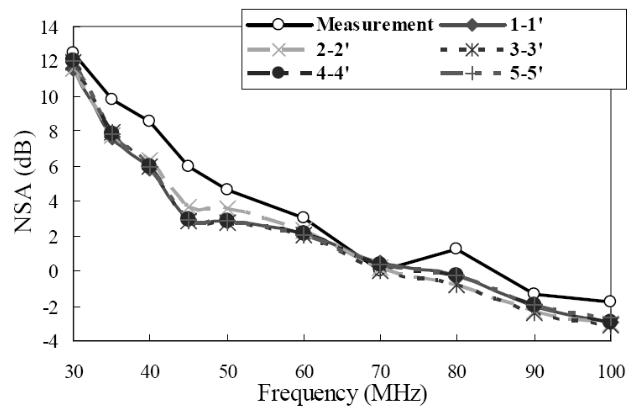

(b) Horizontal polarization

Figure 11: NSA characteristics of semi anechoic chamber.

4.4. Characteristics of Pentagonal Anechoic Chamber

Next, we calculated the characteristics of the pentagonal anechoic chamber, as shown in Figure 12, using the MoM. The base area in the pentagonal anechoic chamber is given as the same that in the rectangular anechoic chamber as shown in Figure 6, and heights of the both chambers are also set as the same value. The reason is to calculate only the modification effect by changing the shape of the anechoic chamber from rectangular to pentagonal. The modeling method of an echoic chamber is similar to that in the case of Figure 6, and the calculation method of antenna factor for the shortened dipole antenna is also similar to that in the case of Figure 7. In this paper, we estimated the fully anechoic chamber using the NSA because we could not calculate the ΔNSA when calculating the NSA using a shortened dipole antenna.

Figure 12 shows the calculation results of the NSA characteristics in the fully anechoic chamber. In Figure 13, "Theory" was calculated as shown in (4).

$$NSA = 20\log_{10}(D) - 20\log_{10}(F) + 32(dB) \tag{4}$$

Where, D is the distance from transmitting to receiving antenna (m) and F is frequency (MHz). (4) is analysis of geometrical optics in free space.

In the vertical polarization as shown in Figure 13(a), the NSA characteristics appeared to be high in the frequency range from 60 to 80 MHz comparing with the Theory. But the maximum difference value between the Theory and the calculation results using MoM is 2 dB, and this value exists in a permissible value. In the horizontal polarization, the NSA characteristics appeared to be high from 30 to 70 MHz, and become almost the same values as the Theory from 60 to 100 MHz. But the maximum difference value between theory and calculation using MoM is 2 dB. The NSA characteristics of both vertical and horizontal polarizations in the pentagonal anechoic chamber are better than that in the rectangular anechoic chamber as shown in Figure 10.

As a result, it is confirmed that the NSA characteristics can be improved by changing to a pentagonal shape in a fully anechoic chamber.

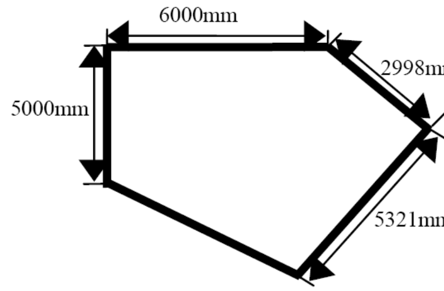

Figure 12: Outline of anechoic chamber.

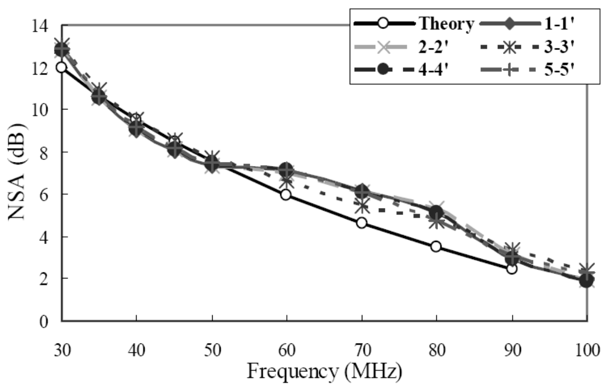

(a) Vertical polarization

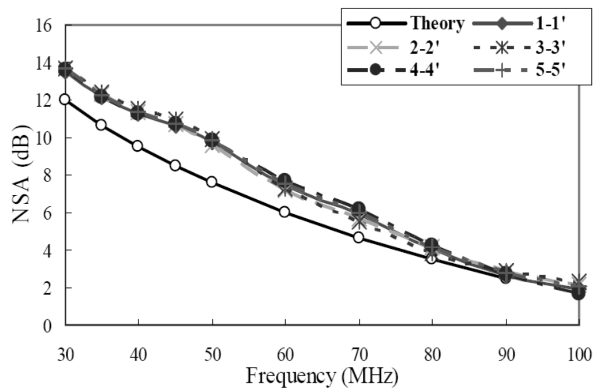

(b) Horizontal polarization

Figure 13: Characteristics of fully anechoic chamber for the pentagonal anechoic chamber.

5. Conclusion

In this paper, we calculated the NSA characteristics of an anechoic chamber using the MoM and compared them with the characteristics using the FDTD method as well as the measured results. The following items were clear.

1 Imitating a wave absorber using wire meshes with limited electric conductivity is effective by controlling the wire interval.

2 The NSA characteristics calculated by using the MoM are more accurate than those using the FDTD method.

3 The NSA characteristics calculated by using the MoM agree with the measured results.

4 Calculation of NSA characteristic using MoM is available in anechoic chamber with compricated shapes.

Future tasks are improvement of calculation accuracy and NSA calculation for the semi anechoic chamber with a pentagonal base.

REFERENCES

1. Inokuchi, M., E. Kimura, and M. Tokuda, "Analyzing and improving characteristics of anechoic chamber using ray tracing method," *Euro EMC 2000*, Session: absorber lined chambers, in Belgium, 2000.
2. Holloway, C. L., P. McKenns, and D. A. Steffen, Finite-difference time-domain modeling for field predictions inside rooms," *IEEE 1997 International Symposium on Electromagnetic Compatibility*, in Austin, 1997.
3. Takiguchi, Y., E. Kimura, and M. Tokuda, "NSA characteristics of anechoic chamber using FDTD method," *4th European Symposium on Electromagnetic Compatibility (EMC Europe 2000 Brugge)*, Vol. 1, 257–262, 2000.
4. Hashimoto, O., "Introductio to wave absober," Morikita Shuppan Co., Ltd., in Japanese, 1997.
5. Voluntary Control Council for Interference by Information Technology Equipment (VCCI), constitutions and regulations, Japanese.

Optimal Grids for the Forward and Inverse Electric Impedance Tomography Problems

F. Guevara Vasquez and L. Borcea
Rice University, USA

V. Druskin
Schlumberger-Doll Research, USA

In Electrical Impedance Tomography (EIT) one seeks to find the conductivity inside a body rom electrical measurements at its surface. This is an ill-posed inverse problem and finding appropriate parametrizations of the unknown is a crucial question.

We begin by reviewing optimal grid results for an 1D inverse problem [1], that gives a rigorous way of choosing an appropriate parameterization of the conductivity. The main idea is to fit the measurements exactly with a resistor network, and to interpret the resistors as local averages of the conductivity over the grid cells of a finite differences discretization. Next, we show how we can profit from a linearization of the resistors to improve over the performance of optimal grids in the 1D EIT forward problem.

Lastly, we discuss a generalization of the 1D methods to the 2D EIT inverse and forward problems, and show numerical results.

REFERENCES

1. Borcea, L., V. Druskin, and L. Knizhnerman., "On the continuum limit of a discrete inverse spectral problem on optimal finite-difference grids," *Comm. Pure Appl. Math*, Vol. LVIII, 1231–1279, 2005.

Finite-difference Solution of the 3D EM Problem Using Integral Equation Type Preconditioners

M. Zaslavsky, **S. Davydycheva**, **V. Druskin**, **L. Knizhnerman**,
A. Abubakar, **and T. M. Habashy**
Schlumberger-Doll Research, USA

The CSEM marine problem requires fine gridding to account for sea bottom bathymetry and to model complicated targets. This results in large computational costs using conventional finite-difference solvers. To circumvent these problems, we employ a volume integral equation approach for preconditioning and to eliminate the background, thus significantly reducing the condition number and dimensionality of the problem. We consider and compare two types of preconditioners, one is based on a magnetic field formulation and the other is based on what is referred to as the dissipative approach by singer. Theory and preliminary numerical results will be presented.

An Effective Inversion Method Based on the Padé via Lanczos Process

R. F. Remis
Delft University of Technology, The Netherlands

Abstract—In this paper we present a nonlinear effective inversion method based on the Padé Via Lanczos process (PVL process). The method finds so-called effective medium parameters of some inhomogeneous object by minimizing an objective function which describes the discrepancy between the scattered field produced by an inhomogeneous object and the scattered field produced by a homogeneous one. This minimization procedure can be carried out by inspection, since the scattered field produced by homogeneous objects can be computed very efficiently using the PVL process. The constant medium parameters of the homogeneous object for which the objective function is minimum are the effective medium parameters we are looking for. A number of numerical experiments are presented in which we illustrate the performance of the method.

1. Introduction

We consider a two-dimensional configuration that is invariant in the z-direction. The position vector in the transverse xy-plane is denoted by x. An object, with known support $\mathbb{S}^{\text{obj}}$, is located in vacuum and is characterized by a conductivity $\sigma(\text{x})$ and a permittivity $\varepsilon(\text{x})$. The object is illuminated by E-polarized waves which are generated by a line source of the form

$$J_z^{\text{ext}}(\text{x}, \omega) = f(\omega)\delta(\text{x} - \text{x}^{\text{src}}), \tag{1}$$

where $f(\omega)$ is the source signature, and the delta function on the right-hand side is the Dirac distribution operative at $\text{x} = \text{x}^{\text{src}}$. The source is located outside the object ($\text{x}^{\text{src}} \notin \mathbb{S}^{\text{obj}}$), and the incident electric field strength generated by the line source is given by

$$E_z^{\text{inc}}(\text{x}, \omega) = \gamma_s H_0^{(1)}(k_0|\text{x} - \text{x}^{\text{src}}|), \tag{2}$$

where $H_0^{(1)}$ is the zero-order Hankel function of the first kind, $\gamma_s = i\omega\mu_0 f(\omega)/4$, and k_0 is the wave number of vacuum.

The total electric field strength is measured at some receiver location $\text{x}^{\text{rec}} \in \mathbb{S}^{\text{obj}}$ and since the incident electric field is known, the scattered electric field strength at the receiver location is known as well. We denote this scattered field by E_z^{sc}. In what follows we assume that this field does not vanish at the receiver location.

The full inversion problem consists of retrieving the conductivity $\sigma(\text{x})$ and permittivity $\varepsilon(\text{x})$ of the object from the measured electric field strength. In our effective inversion method, however, we follow a different approach. We act as if the object is homogeneous and try to find position-independent medium parameters for which the scattered field at the receiver location matches the true scattered field using a well-defined objective function.

Let us be more precise. Introducing the contrast coefficient of the homogeneous object as

$$\zeta(\omega) = \tilde{\varepsilon}_{\text{r}} - 1 + i\frac{\tilde{\sigma}}{\omega\varepsilon_0} \tag{3}$$

where $\tilde{\varepsilon}$ and $\tilde{\sigma}$ are position-independent, we have for the scattered field at the receiver location the integral representation

$$\tilde{E}_z^{\text{sc}}(\text{x}^{\text{rec}}, \omega) = \frac{ik_0^2}{4}\zeta(\omega)\int_{\text{x}' \in \mathbb{S}^{\text{obj}}} H_0^{(1)}(k_0|\text{x}^{\text{rec}} - \text{x}'|)\tilde{E}_z(\text{x}', \omega)dA. \tag{4}$$

This so-called data equation relates the scattered field at the receiver location to the contrast coefficient and the total electric field inside the object. This total field is unknown, but we do know that it satisfies the object equation

$$\tilde{E}_z(\text{x}, \omega) - \frac{ik_0^2}{4}\zeta(\omega)\int_{\text{x}' \in \mathbb{S}^{\text{obj}}} H_0^{(1)}(k_0|\text{x} - \text{x}'|)\tilde{E}_z(\text{x}', \omega)dA = E_z^{\text{inc}}(\text{x}, \omega) \quad \text{with} \quad \text{x} \in \mathbb{S}^{\text{obj}} \tag{5}$$

This object equation is an integral equation of the second kind for the total electric field strength $\tilde{E}_z$ for a given value of the contrast coefficient.

Discretizing the object and data equation on a uniform grid using square discretization cells with side lengths δ is standard and we do not discuss it in this paper. We only give the final forms of the discretized data and object equations, and refer to [1] for details on the discretization process.

After the spatial discretization procedure we obtain the discretized data equation

$$u^{\rm sc}(\zeta) = \gamma_{\rm r}\zeta \mathbf{r}^T \mathbf{u}, \tag{6}$$

where $\gamma_{\rm r} = i(k_0\delta)^2/4$, $\mathbf{r}$ is a receiver vector, and $\mathbf{u}$ is a vector containing the expansion coefficients of the total electric field inside the object. Furthermore, the discretized object equation for the homogeneous object is given by

$$(I - \zeta G)\mathbf{u} = \mathbf{u}^{\rm inc} \tag{7}$$

where I is the identity matrix, and matrix G is a square and symmetric (but not a Hermitean) matrix with (scaled) Green's function values as its entries. Since matrix G results from a discretization of a convolution operator on a uniform grid, we can compute its action on a vector very efficiently using the Fast Fourier Transform (FFT). Finally, the vector $\mathbf{u}^{\rm inc}$ is a vector consisting of incident electric field strength values. This vector can be written in the form $\mathbf{u}^{\rm inc} = \gamma_s \mathbf{s}$ where $\mathbf{s}$ is such that $\mathbf{s} = \mathbf{r}$ if the source and receiver locations coincide. Using the latter form for the incident field vector in the discretized object equation, solving this equation for the total field $\mathbf{u}$, and substituting the result in the discretized data equation, we arrive at

$$u^{\rm sc}(\zeta) = \gamma\zeta \mathbf{r}^T (I - \zeta G)^{-1}\mathbf{s}, \tag{8}$$

with $\gamma = \gamma_{\rm r}\gamma_{\rm s}$. If we compute the scattered field $u^{\rm sc}$ equation (8) directly, we have to solve a forward problem for each new value of ζ. Such a procedure can be computationally intensive and it turns out that it can be avoided using the Padé Via Lanczos (PVL) process. We briefly describe this process in the next section.

2. The Padé via Lanczos Process

We first define our domain of interest. Let $\tilde{\varepsilon}_{\rm r;max}$ and $\tilde{\sigma}_{\rm max}$ be a priori given upper bounds for the constant medium parameters. Then our domain of interest is defined as

$$\mathbb{T} = \{\zeta \in \mathbb{C}; 0 \le {\rm Re}(\zeta) \le \tilde{\varepsilon}_{{\rm r};max} - 1, 0 \le {\rm Im}(\zeta) \le \tilde{\sigma}_{\rm max}/(\omega\varepsilon_0)\},$$

since we require that $\tilde{\varepsilon}_{\rm r} \ge 1$ and $\tilde{\sigma} \ge 0$. We now compute $[k-1/k]$-Padé approximations for the scattered field $u^{\rm sc}$ around an expansion point $\zeta_0 \in \mathbb{T}$ by performing k iterations of the two-sided Lanczos algorithm (see [2]). Matrix factorization is required for any nonzero expansion point and computing such a factorization is expensive (although it has to be computed only once). However, no such factorization is needed if we take $\zeta_0 = 0$ as an expansion point. Only matrix-vector products with matrix G are required in this case and, as we have mentioned above, such products can be computed efficiently using FFT. We therefore construct $[k-1/k]$-Padé approximations for the scattered field $u^{\rm sc}$ around the expansion point $\zeta_0 = 0$ by performing k iterations of the two-sided Lanczos algorithm using the source and receiver vectors s and r as starting vectors. We denote the resulting Padé approximation by $u_k^{\rm sc}$. The crux of the matter is that to evaluate this approximation for each $\zeta \in \mathbb{T}$, we need to solve a k-by-k tridiagonal system and k is typically much smaller than the order of the original discretized object equation. Assuming now that k is such that essentially

$$u_k^{\rm sc}(\zeta) = u^{\rm sc}(\zeta) \quad \text{for all} \quad \zeta \in \mathbb{T},$$

we can conclude that we have an efficient way of evaluating the scattered field for all ζ-values of interest.

3. The Effective Medium Parameters

The effective medium parameters follow from minimizing an objective function defined over the domain of interest. More precisely, the effective medium parameters are defined as those parameters for which the objective function

$$F_1(\zeta) = \frac{|E_z^{\rm sc} - u_k^{\rm sc}|^2}{|E_z^{\rm sc}|^2} \tag{9}$$

attains a minimum in our domain of interest $\mathbb{T}$. If multiple frequency data $E_z^{\rm sc}(\omega_1)$, $E_z^{\rm sc}(\omega_2)$, $\cdots$, $E_z^{\rm sc}(\omega_N)$ is

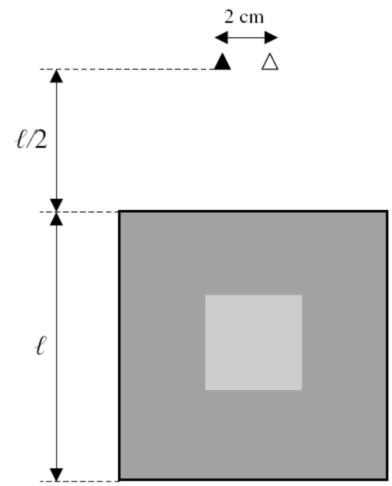

Figure 1: Two-dimensional test configuration.

available, we look for those medium parameters for which the multiple frequency objective function

$$F_N(\zeta) = \sum_{n=1}^{N} \omega_n \frac{|E_z^{\mathrm{sc}}(\omega_n) - u_k^{\mathrm{sc}}(\omega_n)|^2}{|E_z^{\mathrm{sc}}(\omega_n)|^2} \tag{10}$$

is minimum. In the above equation, the weights ω_n satisfy $\sum_{n=1}^{N}\omega_n = 1$. Notice that in the multiple frequency case we have to apply the PVL process for each frequency separately. Moreover, for multiple frequencies the domain of interest on which all the PVL approximations match the true scattered field due to a homogeneous object is taken to be the domain $\mathbb{T}$ which corresponds to the lowest frequency of operation. Minimizing the objective functions can be carried out by inspection since we have a very efficient way of computing the scattered fields $u_k^{\mathrm{sc}}(\omega_n)$. Finally, we mention that we cannot guarantee that the effective medium parameters are unique. The objective function may have multiple minima on the domain of interest and each minimum gives a set of effective medium parameters for the object. However, usually we can overcome the nonuniqueness of the effective medium parameters by including more a priori information, or by performing additional experiments at different frequencies while keeping the source/receiver unit fixed.

4. Numerical Results

We illustrate our effective inversion approach using the two-dimensional configuration shown in Figure 1. A square block with side lengths ℓ is located in a vacuum domain. The block has an inner and an outer part and each part has its own constant medium parameters. Specifically, the outer part has a conductivity σ_1 and a relative permittivity $\varepsilon_{\mathrm{r};1}$, the inner part a conductivity σ_2 and a relative permittivity $\varepsilon_{\mathrm{r};2}$. Obviously, the block is homogeneous if σ_1=σ_2 and $\varepsilon_{\mathrm{r};1} = \varepsilon_{\mathrm{r};2}$. Finally, the source/receiver unit is located a distance $\ell/2$ above the object and the source and the receiver are located 2 cm apart.

In our first example, we operate at a frequency of 36 MHz, and take $\ell = \lambda_{36}$, where λ_{36} is the free-space wavelength corresponding to the operating frequency of 36 MHz. The block is homogeneous with $\sigma_1 = \sigma_2 = 7.5\,\mathrm{mS/m}$ and $\varepsilon_{\mathrm{r};1} = \varepsilon_{\mathrm{r};2} = 5$. For the maximum conductivity and maximum relative permittivity we take $\tilde{\sigma}_{\max} = 10\,\mathrm{mS/m}$ and $\tilde{\varepsilon}_{\mathrm{r};\max} = 6$, respectively. The domain of interest is discrerized on a 50-by-50 grid (leading to 2500 forward problems solved by PVL in less than a second on a notebook with a 1.6 GHz Pentium M processor) and the objective function F_1 on this domain of interest is shown in Figure 2 (left). We observe that the true conductivity and permittivity of the object are recovered. However, a number of additional minima are present near the $\tilde{\varepsilon}_{\mathrm{r}}$-axis. To remove these minima we add two more frequency measurements, namely, one at a frequency of $f = 30$ MHz and one at $f = 42$ MHz. The objective function F_3 for these two frequencies and the frequency of 36 MHz is shown in Figure 2 (right), where we have taken $\omega_n = 1/3$ for $n = 1, 2, 3$. Clearly, the multiple minima have disappeared and a single minimum remains. In addition to using multiple frequency data, we could also change the source and receiver locations. This latter option is not considered in this paper, however.

We now apply our effective inversion method to inhomogeneous blocks. Two blocks of different sizes will be

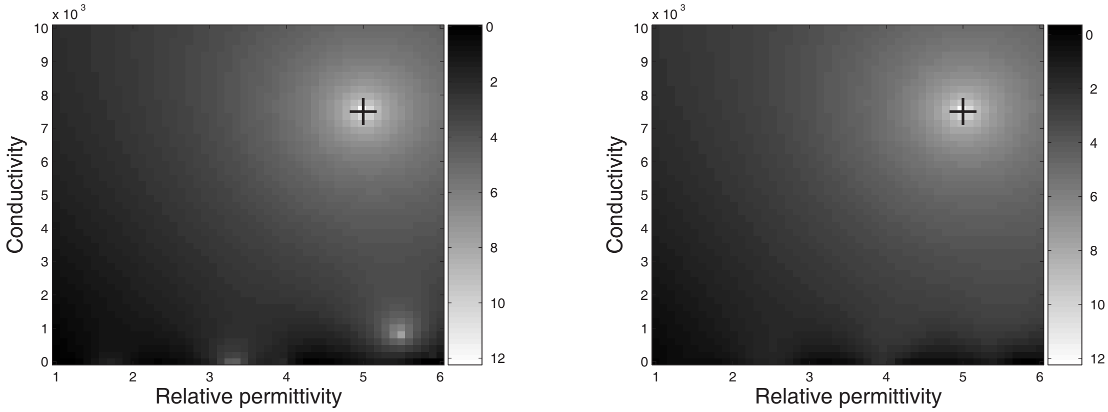

Figure 2: Base 10 logarithm of F_1 (left) and base 10 logarithm of F_3 (right) on the domain of interest.

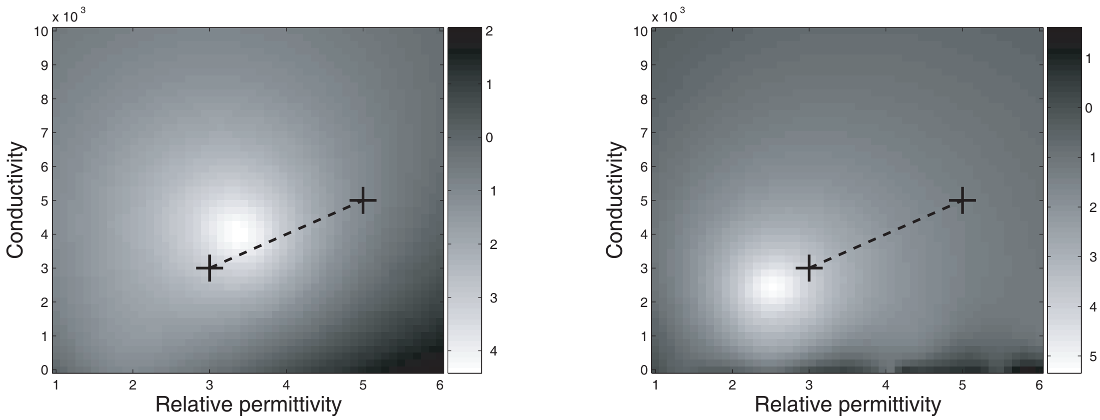

Figure 3: Base 10 logarithm of F_3 for the $\lambda_{36}/4$-block (left) and the λ_{36}-block (right).

considered. The first block has a side length $\ell = \lambda_{36}/4$ and the second one a side length of $\ell = \lambda_{36}$. The outer part of the two blocks has a conductivity $\sigma_1 = 3.0\,\mathrm{mS/m}$ and a relative permittivity $\varepsilon_{\mathrm{r};1} = 3$, while the medium parameters of the inner part are $\sigma_2 = 5.0\,\mathrm{mS/m}$ and $\varepsilon_{\mathrm{r};2} = 5$. For both blocks the area of the inner part is 50% of the total area of the block. Using the same three frequencies as in the previous examples, we obtain the objective functions as shown in Figure 3. The minimum for the $\lambda_{36}/4$-block is located at an acceptable location in the domain of interest, but for the large block the effective medium parameters are smaller than the smallest medium parameters of the block. This result is unexpected. We therefore carried out an additional number of experiments and all these experiments indicate that for inhomogeneous objects it all depends on the size of the object and the sizes of the perturbations with respect to a constant contrast function. This latter function may be large, but the perturbations cannot be "too large". Finding a condition that tells us for which contrast perturbations the proposed method gives reliable results is a topic we are presently investigating. In addition, we want to know how this condition changes if the data is perturbed (by noise, for example) given the magnitude of the data perturbations.

Acknowledgment

The research reported in this paper was supported by a grant of the Netherlands Organization for Scientic Research (NWO).

REFERENCES

1. Richmond, J. H., "Scattering by a dielectric cylinder of arbitrary cross section shape," *IEEE Trans. Antennas Propagat.*, Vol. 13, 334–341, 1965.
2. Feldmann, P. and R. W. Freund, "Efficient linear circuit analysis by Padé approximation via the Lanczos process," *IEEE Trans. Computer-Aided Design*, Vol. 14, No. 5, 639–649, 1995.

Inversion of Large-scale Electromagnetic Data through the Iterative Multizooming Reconstruction of Nonmeasurable Equivalent Current Densities

M. Donelli[1], **D. Franceschini**[1], **M. Benedetti**[1], **A. Massa**[1], **and G. L. Gragnani**[2]

[1]University of Trento, Italy
[2]University of Genoa, Italy

In the framework of the inversion of electromagnetic data, several methodologies consider the introduction of an equivalent current density defined into the dielectric domain to be reconstructed. One of the main drawbacks of these approaches is their "difficulty" to reconstruct the so-called "nonradiating" (or "nonmeasurable") components of the equivalent current density. Hence the obtained solution may suffer from a strong low-pass effect. In order to overcome this drawback, *Habashy et al.*, [1] presented a reconstruction method where the problem of nonmeasurable currents was addressed through a successive steps process. Taking into account the guidelines suggested in [1], *Gragnani et al.*, [2] proposed a nonlinear procedure based on the reconstruction of the measurable components of the equivalent current density by means of the singular value decomposition of the discretized Green's operator. Such components are then inserted into a nonlinear equation whose unknowns are the nonmeasurable components as well as the dielectric properties of the investigation domain. Then, a nonlinear functional is defined and minimized by means of a standard steepest-descent procedure.

Even though the results obtained by taking into account the nonmeasurable current density were better than the ones of the minimum-norm solution, the method demonstrated some inaccuracies or faults due to the presence of the local minima. Moreover, the choice of a suitable representation for the nonradiating currents represented an open problem partially addressed.

In this paper, these problems are faced through an integrated strategy based on an innovative stochastic method and on an iterative multizooming procedure. Since the existence of nonradiating components is equivalent to the Green's integral operator having a null-space and one way to decrease the size of the null space is to let the equivalent current density have fewer degrees of freedom, it is convenient to approximate this density with a smaller number of basis or unknowns, e.g., by using a coarse grid in the domain under test [3]. Consequently, the reconstructed profile presents a poor spatial resolution because of the inappropriate sampling step. Therefore, an iterative multizooming process is considered. Starting from a coarse representation, the method iteratively defines a subgridding of the support of the equivalent current density successively improving the representation of the current by minimizing the nonlinear cost function defined in [2]. In order to avoid local minima problems, an innovative minimization technique based on the particle swarm optimizer (PSO) [4] is used.

REFERENCES

1. Habashy, T. M., M. L. Oristaglio, and A. T. de Hoop, "Simultaneous nonlinear reconstruction of two-dimensional permittivity and conductivity," *Radio Sci.*, Vol. 29, 1101–1118, 1994.
2. Gragnani, G. L. and S. Caorsi, "Inverse-scattering method for dielectric objects based on the reconstruction of nonmeasurable equivalent current density," *Radio Sci.*, Vol. 34, 1–8, 1999.
3. Chew, W. C., Y. M. Wang, G. P. Otto, D. Lesselier, and J. Ch. Bolomey, "On the inverse source method of solving inverse scattering problems," *Inverse Probl.*, Vol. 10, 547–553, 1994.
4. Donelli, M. and A. Massa, "A computational approach based on a particle swarm optimizer for microwave imaging of two-dimensional dielectric scatterers," *IEEE Trans. Microwave Theory Techn.*, Vol. 53, 1761–1776, 2005.

QN Inversion of Large-scale MT Data

A. D. Avdeeva[1], **and D. B. Avdeev**[1,2]
[1]Dublin Institute for Advanced Studies, Ireland
[2]IZMIRAN, Russian Academy of Sciences, Russia

Abstract—A limited memory quasi-Newton (QN) method with simple bounds is applied to a 1-D magnetotelluric (MT) problem. The method is used to invert a realistic synthetic MT impedance dataset, calculated for a layered earth model. An adjoint method is employed to calculate the gradients and to speed up the inverse problem solution. In addition, it is shown that regularization stabilizes the QN inversion result. We demonstrate that only a few correction pairs are enough to produce reasonable results. Comparison with inversion based on known L-BFGS-B optimization algorithm shows similar convergence rates. The study presented is a first step towards the solution of large-scale electromagnetic problems with a full 3-D conductivity structure of the Earth.

1. Introduction

Quasi-Newton (QN) methods have become a very popular tool for the numerical solution of electromagnetic (EM) inverse problems (see [8, 7]). The reasoning behind it is that the method requires calculation of gradients only, while at the same time avoiding calculations of second-derivative terms. However, even with the gradients only, the QN methods may require excessively large computational time if the gradients are calculated straightforwardly. An effective way to calculate the gradients is delivered by an adjoint method (see [11, 4]). Also, for large-scale inverse problems the limited memory QN methods have to be applied, since their requirements for storage are not so excessive as for other QN methods. In this paper, as a first step to solving the 3-D EM case, we have applied a limited memory QN method for constrained optimization to solve 1-D magnetotelluric (MT) problems. This optimization method is an extension of previous work [9]. As distinct from this earlier work we implement the Wolfe conditions to terminate the line search procedure, as was recommended in [3]. First we present a simple review of the limited memory QN method for inversion of 1-D MT data. Then, we demonstrate the efficiency of our inversion on a synthetic, but realistic numerical example, along with a comparison with inversion based on the L-BFGS-B optimization method introduced by [3]. The results presented are encouraging and suggest that the method has the potential to handle the more geophysically realistic 3-D inverse problem.

2. 1-D MT Inversion

In the frame of the magnetotelluric method both the electric and magnetic fields are recorded. These fields are then processed to calculate the observed impedance dataset. This dataset is finally inverted to derive a distribution of electrical conductivity in the earth.

Thus, for 1-D MT inversion a layered earth model is considered and conductivities of the layers are sought. This problem is usually solved by minimization of the following objective function

$$\varphi(\mathbf{m},\lambda) = \varphi_d(\mathbf{m}) + \lambda\varphi_s(\mathbf{m}) \underset{\mathbf{m}}{\longrightarrow} \min, \tag{1}$$

where $\varphi_d(\mathbf{m}) = \frac{1}{2}\sum\limits_{j=1}^{M} \alpha_j \left|Z_j - d_j\right|^2$ is the data misfit. Here $\mathbf{m} = (m_1, ..., m_N)^T$ is the vector consisting of the electrical conductivities of the layers; superscript T means transpose; N is the number of the layers; $Z_j(\mathbf{m})$ and d_j are the complex-valued modeled and observed impedances at the j-th period ($j = 1, ..., M$) respectively; $\alpha_j = \frac{2}{M}\epsilon_j^{-2}\left|d_j\right|^{-2}$ are the positive weights; ϵ_j is the relative error of the impedance $Z_j(\mathbf{m})$ and λ is a Lagrange multiplier. Our choice of λ is a simple variant of an algorithm presented in [6]. As prescribed by the regularization theory (see [12]), the function (1) has a regularized part (a stabilizer) $\varphi_s(\mathbf{m})$. This stabilizer can be chosen by many ways, and moreover, the correct choice of $\varphi_s(\mathbf{m})$ is crucial for a reliable inversion. However, this aspect of the problem is out of the scope of this paper. We consider the following stabilizer (see [5]) $\varphi_s(\mathbf{m}) = \sum\limits_{i=2}^{N}\left(\frac{m_i}{m_i^0} - \frac{m_{i-1}}{m_{i-1}^0}\right)^2$, where $\mathbf{m}^0 = (m_1^0, ..., m_N^0)^T$ is an initial guess model. It is of importance that, as the conductivities $m_i\,(i = 1, \ldots, N)$ must be non-negative and realistic, the optimization problem (1) is subject to bounds

$$l_i \le m_i \le u_i, \tag{2}$$

where l_i and u_i are the lower and upper bounds, respectively and $l_i \geq 0\,(i = 1, \ldots, N)$.

A limited memory quasi-Newton method. We notice that the problem posed in (1)– (2) is a typically constrained optimization problem with simple bounds. To solve this problem Newton-type iterative methods are commonly applied. However, most of these methods are not applicable to large-scale optimization problems because the storage and computational requirements become excessive. To overcome this, a limited memory quasi-Newton method has been developing (see [10] for a good introduction). Let us now describe our implementation of such a technique.

At each iteration step k the search direction, vector $\mathbf{p}^{(k)}$, is calculated as $\mathbf{p}^{(k)} = -\mathbf{G}^{(k)}\mathbf{g}^{(k)}$, where the symmetric matrix $\mathbf{G}^{(k)}$ is an approximation to the inverse Hessian matrix and $\mathbf{g}^{(k)}$ is the gradient $\mathbf{g} = (\frac{\partial\varphi}{\partial m_1}, \ldots, \frac{\partial\varphi}{\partial m_N})^T$ calculated at $\mathbf{m} = \mathbf{m}^{(k)}$. An explicit expression for the matrix $\mathbf{G}^{(k)}$ is given in [10, p. 225, formula (9.5)]. It is important that the matrix $\mathbf{G}^{(k)}$ is stored implicitly using n_{cp} correction pairs $\{\mathbf{s}^{(n)}, \mathbf{y}^{(n)}\}$ $(n = k - n_{cp}, \ldots, k-1)$ previously computed as $\mathbf{s}^{(n)} = \mathbf{m}^{(n+1)} - \mathbf{m}^{(n)}$, $\mathbf{y}^{(n)} = \mathbf{g}^{(n+1)} - \mathbf{g}^{(n)}$. The main idea behind this approach is to use information from only the most recent iterations and the information from earlier iterations is discarded in the interests of saving storage. In [10, p. 225] it is advocated that n_{cp} between 3 and 20 may produce satisfactory results.

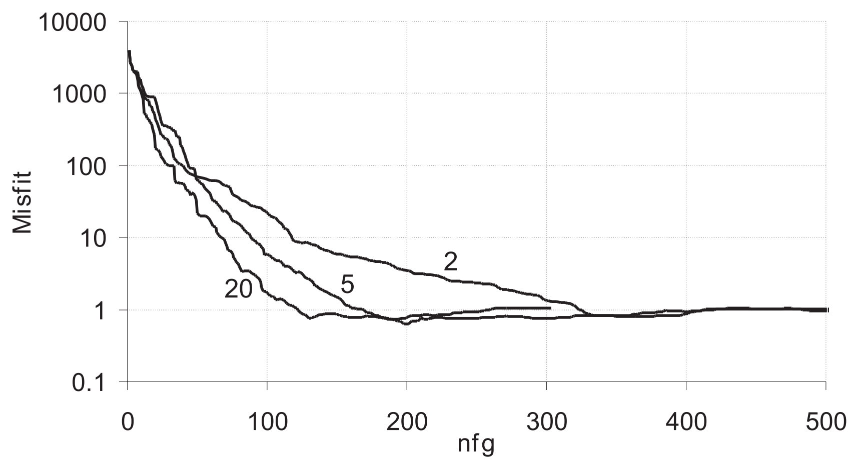

Figure 1: Comparison of LMQNB inversions for 2, 5 and 20 correction pairs.

The next iterate $\mathbf{m}^{(k+1)}$ is then found as $\mathbf{m}^{(k+1)} = \mathbf{m}^{(k)} + \alpha^{(k)}\mathbf{p}^{(k)}$, where the step length $\alpha^{(k)}$ is computed by an inexact line search procedure. This procedure finds a step length that delivers an adequate decrease in the objective function φ along the search direction $\mathbf{p}^{(k)}$. Let us demonstrate how in our implementation we provide the positive definiteness of the matrix $\mathbf{G}^{(k)}$, required to guarantee the descent direction $\mathbf{p}^{(k)}$. When the vectors $\mathbf{s}^{(k-1)}$ and $\mathbf{y}^{(k-1)}$ satisfy the curvature condition $\mathbf{s}^{(k-1)T}\mathbf{y}^{(k-1)} > 0$, it can be shown that the matrix $\mathbf{G}^{(k)}$ is positive definite. This condition is guaranteed to hold if we use the Wolfe conditions (see [10]) to terminate the line search. But the Wolfe conditions may not be reached inside the feasible region defined within the bounds set by equation (2). In this case, we modify $\mathbf{s}^{(k-1)}$ as prescribed in [9, p. 1513] to guarantee that matrix $\mathbf{G}^{(k)}$ is positive definite.

Alternative ways to deal with such boundary constrained QN optimization can be found in [3].

Speeding up the solution. As presented above, at each iteration step k the inverse problem solution requires calculating the gradient $\mathbf{g}^{(k)}$. However for large-scale problems (when N is large) a straightforward calculation may be prohibitive in terms of computational time. One can significantly speed up the calculation by using an adjoint method (see [11, 4]). We have applied such a method to the 1-D MT case. The derivatives are numerically calculated as $\frac{\partial\varphi_d}{\partial\sigma_i} = -Re\left(\sum_{j=1}^{M}\alpha_j\Gamma_{ij}\left(\overline{Z_j} - \overline{d_j}\right)Z_j^2\right)$, where $i = 1, \ldots, N$, the sign Re means the real part of its complex argument and all the coefficients Γ_{ij} are found by solving a single adjoint forward problem. Thus, our calculation of the gradient requires the solution of a single forward and adjoint problem. This approach may be extended with some effort to the 3-D case. It is also noteworthy that for the 1-D MT case the gradient can also be calculated using the chain-rule (see [5]).

We have therefore implemented the limited memory QN method with simple bounds (hereinafter, referred as LMQNB), which is described above. It should be noted here that our implementation differs from that of [9], in that the LMQNB uses the Wolfe conditions to terminate the line search.

3. Model Examples

Let us study on a synthetic 1-D MT example the convergence rate of the LMQNB inversion for a various number n_{cp} of correction pairs. A 7-layered earth model (see Fig. 3) was compiled from the models (see [1]) derived from a seafloor MT and a global GDS long-period dataset collected in the North Pacific Ocean. To complicate the inversion process we subdivided the three upper layers in this model (to depth of 394 km) into 197 equally thick sublayers ($N = 197$). For this 201-layered model we inverted the impedance $d_j = Z_j(\mathbf{m})$ calculated at $M = 30$ periods from 10 s to 10800 s.

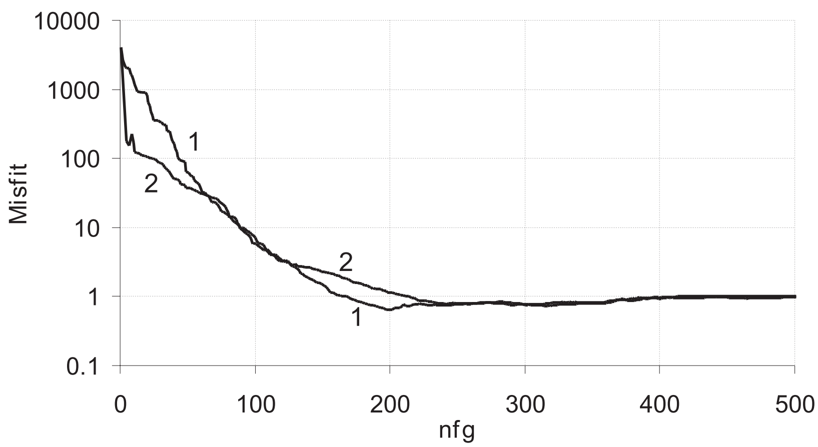

Figure 2: Comparison of inversions based on the LMQNB (1) and L-BFGS-B (2) optimisations with $n_{cp} = 5$ and $\lambda = 320$.

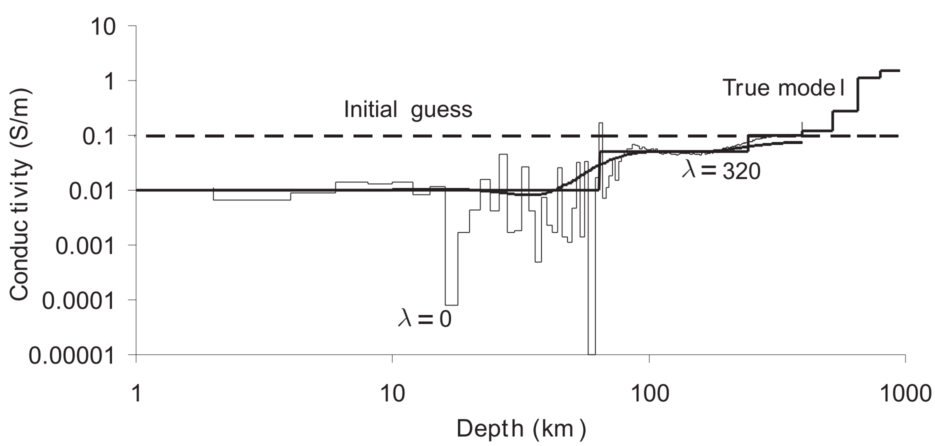

Figure 3: The conductivity models obtained from inversion based on the LMQNB optimization with $n_{cp} = 5$ for $\lambda = 0$ and $\lambda = 320$. The true model is shown by the solid line and the initial guess by the dashed line.

In addition, we added 0.5% random noise to the impedance data. The relative error ϵ_j (see α_j on page 1) of the impedance was taken as 0.01. A 10 ohm-m uniform half-space was used as an initial guess $\mathbf{m} = \mathbf{m}^0$. The convergence rate curves are shown in Fig. 1 as a function of the total number (n_{fg}) of function φ and gradient $\mathbf{g}$ evaluations for $\lambda = 320$. It is surprising that so small a number of pairs ($n_{cp} = 5$) can be chosen sufficiently to get a relatively reasonable result.

Let us again consider the 201-layered model and the dataset, described in the previous example. In our next example (see Fig. 2) we present a comparison of two solutions of a 1-D MT inverse problem. The first solution is based on the optimization method offered in this paper and the second one exploits the L-BFGS-B optimization code from [3]. The comparison is presented for $n_{cp} = 5$ correction pairs and for $\lambda = 0$ and $\lambda = 320$. Both solutions converge in a similar way and also produce similar models. The inversion results are presented in Fig. 3.

4. Conclusion

This paper described a limited memory QN method applied to solve a 1-D MT inverse problem. The method is also valid for large-scale problems, and may be equally applied for 1-D, 2-D, or 3-D MT cases. In the numerical examples presented we have demonstrated that a few correction pairs are enough to obtain reasonable inversion results. To speed-up the inversion the adjoint method has been applied to calculate the gradients. The non-trivial problem of such a calculation of gradients in the 3-D MT case is presented in a companion paper [2]. Another finding of our numerical experiments is that the LMQNB solution converges similarly to the solution based on the L-BFGS-B method introduced in [3].

Acknowledgment

This work was carried out in the Dublin Institute for Advanced Studies and was supported by the Cosmogrid project, which is funded by the Programme for Research in Third Level Institutions under the National Development Plan and with assistance from the European Regional Development Fund. Thanks to Brian O'Reilly for corrections to English. We acknowledge helpful comments of an anonymous reviewer. AA also acknowledges the constructive support of her supervisors Alan Jones and Colin Brown.

REFERENCES

1. Avdeev, D. B., H. Utada, A. V. Kuvshinov, and T. Koyama, "Three-dimensional electromagnetic modeling of the Hawaiian swell," *AGU Fall Meeting, 13-17 December, San Francisco, CA*, F630, 2004.
2. Avdeev, D. B. and A. D. Avdeeva, "A rigorous 3-D MT inversion," this volume.
3. Byrd, R. H., P. Lu, J. Nocedal, and C. Zhu, "A limited memory algorithm for bound constrained optimization," *SIAM J. Scientific Computing*, Vol. 16, 1190–1208, 1995.
4. Chen, J., D. W. Oldenburg, and E. Haber, "Reciprocity in electromagnetics: application to modeling marine magnetometric resistivity data," *Phys. Earth Planet. Inter.*, Vol. 150, 45–61, 2005.
5. Constable, S. C., R. L. Parker, and C. G. Constable, "Occam's inversion: a practical algorithm for generating smooth models from electromagnetic sounding data," *Geophysics*, Vol. 52, 289–300, 1987.
6. Haber, E. and D. W. Oldenburg, "Joint inversion: a structural approach," *Inverse Problems*, Vol. 13, 63–77, 1997.
7. Haber, E., "Quasi-Newton methods for large-scale electromagnetic inverse problems," *Inverse Problems*, Vol. 21, 305–323, 2005.
8. Newman, G. A. and P. T. Boggs, "Solution accelerators for large-scale three-dimensional electromagnetic inverse problem," *Inverse Problems*, Vol. 20, s151–s170, 2004.
9. Ni, Q. and Y. Yuan, "A subspace limited memory quasi-Newton algorithm for large-scale nonlinear bound constrained optimization," *Mathematics of Computation*, 66/220, 1509–1520, 1997.
10. Nocedal, J. and S. J. Wright, *Numerical Optimization*, Springer, 1999.
11. Rodi, W. and R. L. Mackie, "Nonlinear conjugate gradients algorithm for 2-D magnetotelluric inversion," *Geophysics*, Vol. 66, 174–187, 2001.
12. Tikhonov, A. N. and V. Y. Arsenin, *Solutions of Ill-posed Problems*, Wiley, New York, 1977.

2.5D Algorithm for Tomographic Imaging of the Deep Electromagnetic Geophysical Measurement

A. Abubakar, **T. M. Habashy**, **V. Druskin**, **D. Alumbaugh**, **P. Zhang**
M. Wilt, **and L. Knizhnerman**
Schlumberger, USA

Abstract—We present a 2.5D inversion algorithm for the interpretation of electromagnetic data collected in a cross-well configuration. Some inversion results from simulated data as well as from field measurements are presented in order to show the efficiency and the robustness of the algorithm.

1. Introduction

Electromagnetic methods are essential tools for the appraisal of a reservoir because of their sensitivity to the resistivity (conductivity) which is a function of the fluid saturation. One of the traditional electromagnetic techniques for well logging is the induction single-well measurement. This technique is employed both as a wireline technology and as a measurement while drilling to estimate near well-bore resistivity. This induction logging measurement has a sensitivity of up to a few meters from the well and is a function of the separation between the transmitter and receiver and frequency of operation.

To reach deeper into the reservoir, a cross-well electromagnetic induction technology was developed, see Wilt et al., [6] and Spies and Habashy [4]. The system operates very similar to the single-well logging tool however with transmitter and receiver deployed in separate wells. During a cross-well survey the receivers are lowered into one well, initially to the bottom of the survey-depth interval. Then the transmitter is lowered into the second well and is moved to log the entire survey-depth interval. During logging the transmitter broadcasts electromagnetic signals at a number of pre-prescribed frequencies while at the receiver well these signals are recorded. After the transmitter run is completed the receiver array is moved to the next depth station in the survey interval and the process is then repeated until the entire depth interval has been covered. After the data set has been collected, an inversion process is applied to convert the electromagnetic signals to a resistivity distribution map of the region between the wells. Furthermore, since most of the survey involves only two wells, one can usually assume in the inversion that the geometry is 2D (the resistivity distribution is invariant along the direction perpendicular to the plane containing the wells).

This inverse process is one of the most challenging parts of the effort to make this cross-well technology work since it requires one to solve a full nonlinear inverse scattering problem, which is usually ill-conditioned and non-unique. Moreover, when the number of the model parameters to be inverted is large, the inversion can be very time-consuming.

In order to carry out the inversion within a reasonable time, we employ a finite-difference code as a forward simulator. In this forward code the configuration is numerically discretized using a small number of cells determined by the optimal grid technique, see Ingerman et al. [3]. The resulting linear system of equations representing the discretized forward problem has to be solved in each inversion step. To solve this system, we use a LU decomposition method that allows us to obtain the solution for all transmitters simultaneously. Furthermore, in order to be able to use the optimal grid without sacrificing accuracy we use an anisotropic material averaging formula. All these features help in reducing the computational time for constructing sensitivity kernel and for calculating the data misfit.

For the inversion method, we employ a constrained Gauss-Newton minimization scheme (see Habashy and Abubakar [2]) where the inverted model parameters are forced to lie within their physical bounds by using a nonlinear transformation procedure. We further enforce a reduction in the cost function after each iteration by employing a line search method. To improve on the conditioning of the inversion problem, we use two different regularizers. The first is a traditional L_2-norm regularizer, which allows a smooth solution. The second is the so-called weighted L_2-norm regularizer, which can provide a sharp reconstructed image, see van den Berg and Abubakar in [5]. The trade-off parameter which provides the relative weighting between the data and the regularization part of the cost function is determined automatically to enhance the robustness of the method. We will present results from simulated data as well as from field measurements to demonstrate the capabilities of the developed algorithm.

2. Methodology

We consider a general discrete nonlinear inverse problem described by the operator equation

$$\overline{\mathbf{d}}^{\text{obs}} = \overline{\mathbf{S}}\,(\overline{\mathbf{m}}), \tag{1}$$

where $\overline{\mathbf{d}}^{\text{obs}} = [d_1^{\text{obs}}\, d_2^{\text{obs}} \,\ldots\, d_J^{\text{obs}}]^T$ is the vector of measured data and $\overline{\mathbf{S}} = [S_1\, S_2 \,\ldots\, S_J]^T$ is the vector of data computed for the model parameters $\overline{\mathbf{m}} = [m(x_q, z_r),\ q = 1, 2, \ldots, Q;\ r = 1, 2, \ldots, R]$, where x_q and z_r denote the center of the 2D discretization cell. We use a lexicographical ordering of the unknowns to map the 2D array indices to 1D column indices $(q, r) \to R \times (q-1) + r$. The superscript ^{T} denotes the transpose of a vector. We assume that there are J number of data points in the experiment and that the configuration can be described by $I = Q \times R$ model parameters. In this cross-well electromagnetic problem the data are the component of the magnetic field which is parallel to the borehole axis. The unknown model parameter $m(\overline{\mathbf{r}}) = \sigma(\overline{\mathbf{r}})/\sigma_0$ is the normalized conductivity where σ_0 is a constant conductivity. In the implementation σ_0 is chosen to be the average of the initial model used in the inversion.

We pose the inversion as the minimization problem. Hence at the n^{th} iteration we reconstruct $\overline{\mathbf{m}}_n$ that minimizes

$$\Phi_n(\overline{\mathbf{m}}) = \phi^d(\overline{\mathbf{m}}) + \lambda_n \phi_n^m(\overline{\mathbf{m}}), \tag{2}$$

where ϕ^d is a measure of data misfit:

$$\phi^d(\overline{\mathbf{m}}) = \frac{\sum_{j=1}^{J} \left| W_{j,j}[d_j^{\text{obs}} - S_j(\overline{\mathbf{m}})] \right|^2}{\sum_{j=1}^{J} \left| W_{j,j}\, d_j^{\text{obs}} \right|^2}, \tag{3}$$

in which $|\cdot|$ denotes the absolute value and $\overline{\overline{\mathbf{W}}}$ is a diagonal matrix whose elements are the estimates of the standard deviations of the noise. The symbol λ denotes the regularization parameter and ϕ^m is a measure of the variation in the geometrical configuration:

$$\phi_n^m(\overline{\mathbf{m}}) = \int_D \mathrm{d}\overline{\mathbf{r}}\, b_n^2(\overline{\mathbf{r}}) \left\{ \left| \nabla [m(\overline{\mathbf{r}}) - m^{\text{ref}}(\overline{\mathbf{r}})] \right|^2 + \delta_n^2 \right\}, \tag{4}$$

where $\nabla = [\partial_x\, \partial_z]^T$ denotes spatial differentiation with respect to $\overline{\mathbf{r}} = [x\, z]^T$, and the weight $b_n^2(\overline{\mathbf{r}})$ is given by

$$b_n^2(\overline{\mathbf{r}}) = \frac{1}{\displaystyle\int_D \mathrm{d}\overline{\mathbf{r}} \left| \nabla [m_n(\overline{\mathbf{r}}) - m^{\text{ref}}(\overline{\mathbf{r}})] \right|^2 + \delta_n^2} \tag{5}$$

for the L_2-norm regularizer and

$$b_n^2(\overline{\mathbf{r}}) = \frac{1}{V} \frac{1}{\left| \nabla [m_n(\overline{\mathbf{r}}) - m^{\text{ref}}(\overline{\mathbf{r}})] \right|^2 + \delta_n^2} \tag{6}$$

for the weighted L_2-norm regularizer introduced in van den Berg and Abubakar [5]. The symbol $V = \int_D \mathrm{d}\overline{\mathbf{r}}$ denotes the volume of the computational domain and $\overline{\mathbf{m}}^{\text{ref}}$ is the known reference model. Note that for the L_2-norm regularizer the weight $b_n^2(\overline{\mathbf{r}})$ is independent of the spatial position $\overline{\mathbf{r}}$. The δ_n^2 is a constant which is chosen to be equal to: $\delta_n^2 = \phi^d(\overline{\mathbf{m}}_n)/(\Delta_x \Delta_z)$, where Δ_x and Δ_z are the widths of the discretization cell. The regularization parameter λ is determined automatically using the technique described in Habashy and Abubakar [2].

To solve (2) we employ a Gauss-Newton minimization approach. At the n^{th} iteration we obtain a set of linear equations for the search vector $\overline{\mathbf{p}}_n$ that identifies the minimum of the approximated quadratic cost function, namely,

$$\overline{\overline{\mathbf{H}}}_n \cdot \overline{\mathbf{P}}_n = -\overline{\mathbf{g}}_n, \tag{7}$$

where

$$\overline{\overline{\mathbf{H}}}_n = \overline{\overline{\mathbf{J}}}_n^T \cdot \overline{\overline{\mathbf{W}}}^T \cdot \overline{\overline{\mathbf{W}}} \cdot \overline{\overline{\mathbf{J}}}_n^T + \lambda_n \overline{\overline{\mathcal{L}}}(\overline{\mathbf{m}}_n), \tag{8}$$

$$\overline{\mathbf{g}}_n = \overline{\overline{\mathbf{J}}}_n^T \cdot \overline{\overline{\mathbf{W}}}^T \cdot \left[\overline{\mathbf{d}}^{\text{obs}} - \overline{\mathbf{S}}(\overline{\mathbf{m}}_n) \right] - \lambda_n \overline{\overline{\mathcal{L}}}(\overline{\mathbf{m}}_n) \cdot \overline{\mathbf{m}}_n, \tag{9}$$

in which

$$\overline{\overline{\mathcal{L}}}(\overline{\mathbf{m}}_n) \cdot \overline{\mathbf{m}}_n = \nabla \cdot [b_n^2(\overline{\mathbf{r}})\, \nabla_{m_n}(\overline{\mathbf{r}})]. \tag{10}$$

In (8) and (9), $\overline{\overline{\mathbf{J}}}_n = \overline{\overline{\mathbf{J}}}(\overline{\mathbf{m}}_n)$ is the $J \times I$ Jacobian matrix and is given by the following expression:

$$J_{j,i;n} = \eta \frac{\partial S_j(\overline{\mathbf{m}}_n)}{\partial m_{i;n}}, \qquad \eta = \frac{1}{\sum_{k=1}^{J} |W_{k,k}\, d_k^{\text{obs}}|^2}. \tag{11}$$

This Jacobian matrix is calculated using an adjoint formulation, which only needs an extra forward problem solution at each Gauss-Newton search step. In this extra forward problem solution the roles of the transmitters and receivers are interchanged. However since we are using a 2.5D forward code with a LU decomposition solver, we need only one forward call to calculate both the data misfit and to generate the Jacobian matrix. Note that the use of the direct solver is possible, since we reduced the number of grids outside the inter-well region by employing the optimal grid technique in Ingerman et al. [3]. Furthermore, in order to be able to use the optimal grids without scarifying accuracy we use an anisotropic homogenization technique.

Since the size of the Hessian matrix $\overline{\overline{\mathbf{H}}}_n$ is large, we solve the linear system of equations (7) using a linear iterative method. To that end we first rewrite equation (7) as follows:

$$\overline{\overline{\mathcal{K}}} \cdot \overline{\mathbf{p}}_n = \bar{\mathbf{f}}, \tag{12}$$

where $\overline{\overline{\mathcal{K}}} = \overline{\overline{\mathbf{H}}}_n$ and $\bar{\mathbf{f}} = -\overline{\mathbf{g}}_n$. Since $\overline{\overline{\mathcal{K}}}$ is a self adjoint matrix, we employ a Conjugate Gradient Least Square (CGLS) scheme to solve this linear system of equations. This CGLS scheme starts with the initial values:

$$\bar{\mathbf{r}}^{(0)} = \bar{\mathbf{f}} - \overline{\overline{\mathcal{K}}} \cdot \overline{\mathbf{p}}_n^{(0)},\ \text{ERR}^{(0)} = \frac{||\bar{\mathbf{r}}^{(0)}||}{||\bar{\mathbf{f}}||}, \tag{13}$$

where $\overline{\mathbf{p}}_n^{(0)} = \overline{\mathbf{p}}_{n-1}$. Next, we compute successively for $N = 1, 2, \ldots,$

$$\begin{aligned}
A^{(N)} &= <\bar{\mathbf{r}}^{(N-1)},\ \overline{\overline{\mathcal{K}}} \cdot \bar{\mathbf{r}}^{(N-1)}>, \\
\overline{\mathbf{u}}^{(N)} &= \bar{\mathbf{r}}^{(N-1)},\ N = 1, \\
&= \bar{\mathbf{r}}^{(N-1)} + \frac{A^{(N)}}{A^{(N-1)}} \overline{\mathbf{u}}^{(N-1)},\ N > 1, \\
B^{(N)} &= ||\overline{\overline{\mathcal{K}}} \cdot \overline{\mathbf{u}}^{(N)}||^2, \\
\overline{\mathbf{p}}_n^{(N)} &= \overline{\mathbf{p}}_n^{(N-1)} + \frac{A^{(N)}}{B^{(N)}} \overline{\mathbf{u}}^{(N)}, \\
\bar{\mathbf{r}}^{(N)} &= \bar{\mathbf{f}} - \overline{\overline{\mathcal{K}}} \cdot \overline{\mathbf{p}}_n^{(N)},\ \text{ERR}^{(N)} = \frac{||\bar{\mathbf{r}}^{(N)}||}{||\bar{\mathbf{f}}||},
\end{aligned} \tag{14}$$

where $||\overline{\mathbf{u}}|| = \sqrt{<\overline{\mathbf{u}}, \overline{\mathbf{u}}>}$ denotes the L_2-norm of a vector. This CGLS iteration process stops if the relative error $\text{ERR}^{(N)}$ reaches a prescribed value, or when the total number of iterations N exceeds a prescribed maximum.

After the search vector $\overline{\mathbf{p}}_n = \overline{\mathbf{p}}_n^{(N)}$ has been obtained, the unknown model parameters are updated as follows:

$$\overline{\mathbf{m}}_{n+1} = \overline{\mathbf{m}}_n + \nu_n \overline{\mathbf{p}}_n, \tag{15}$$

where ν_n is a scalar constant parameter to be determined by a line search algorithm. In the implementation we always try first the full step, i.e., $\nu_n = 1$, and check if it reduced the value of the cost function Φ_n. If not, we backtrack along the Gauss-Newton step until we have an acceptable step. Since the Gauss-Newton step is a descent direction for Φ_n, we are guaranteed to find an acceptable step. In this procedure ν_n is selected such that:

$$\Phi_n(\overline{\mathbf{m}}_n + \nu_n \overline{\mathbf{p}}_n) \leq \Phi_n(\overline{\mathbf{m}}_n) + \alpha \nu_n \delta\Phi_{n+1}, \tag{16}$$

where $0 < \alpha < 1$ is a fractional number, which is set to be quite small, i.e., α to 10^{-4}, so that hardly more than a decrease in cost function value is required (see Dennis and Schnabel [1]). The parameter $\delta\Phi_{n+1}$ is the rate of decrease of $\phi(\overline{\mathbf{m}})$ at $\overline{\mathbf{m}}_n$ along the direction $\overline{\mathbf{p}}_n$ and is given by:

$$\delta\Phi_{n+1} = \frac{\partial}{\partial \nu} \Phi_n(\overline{\mathbf{m}}_n + \nu \overline{\mathbf{p}}_n)\Big|_{\nu=0} = \overline{\mathbf{g}}_n^T \cdot \overline{\mathbf{p}}_n. \tag{17}$$

If, at the $(n+1)^{\text{th}}$ iteration, $\nu_n^{(m)}$ is the current step-length that does not satisfy the condition (16), we compute the next backtracking step-length, $\nu_n^{(m+1)}$, by searching for the minimum of the cost function assuming a quadratic approximation in ν. Hence $\nu_k^{(m+1)}$ for $m = 0, 1, 2, \ldots$ is given by:

$$\nu_n^{(m+1)} = \frac{-0.5\left[\nu_k^{(m)}\right]^2 \delta\Phi_{(n+1)}}{\Phi_n(\overline{\mathbf{m}}_n + \nu_n^{(m)}\overline{\mathbf{p}}_n) - \Phi_n(\overline{\mathbf{m}}_n) - \nu_n^{(m)}\delta\Phi_{n+1}}. \tag{18}$$

In general, it is not desirable to decrease $\nu_n^{(m+1)}$ too much since this may excessively slow down the iterative process. To prevent this slow down, we set $\nu_n^{(m+1)} = 0.1\nu_n^{(m)}$ if $\nu_n^{(m+1)} < 0.1\nu_n^{(m)}$ (but with ν_n not to decrease below 0.1, i.e., $\nu_{\min} = 0.1$ to guard against a too small value of ν) and then proceed with the Gauss-Newton step.

To impose *a priori* information of maximum and minimum bounds on the unknown parameters, we constrained them using a nonlinear transformation of the form:

$$m_i = \frac{m_i^{\max} + m_i^{\min}}{2} + \frac{m_i^{\max} - m_i^{\min}}{2}\sin(c_i), \tag{19}$$

where $m_i^{\max}$ and $m_i^{\min}$ are upper and lower bounds on the physical model parameter m_i. It is clear that $m_i \to m_i^{\min}$, as $\sin(c_i) \to -1$ and $m_i \to m_i^{\max}$, as $\sin(c_i) \to +1$. This nonlinear transformation will force the reconstruction of the model parameters to lie always within their prescribed bounds. Formally by using this nonlinear transformation we should be updating the auxiliary unknown parameters c_i instead of the model parameters m_i. However by using the relation $p_i = q_i\, \mathrm{d}m_i/\mathrm{d}c_i$ where q_i is the Gauss-Newton search step with respect to c_i, we obtain the following relationships between the two successive iterates $m_{i,n+1}$ and $m_{i,n}$ of m_i:

$$m_{i,n+1} = \frac{m_i^{\max} + m_i^{\min}}{2} + \alpha_n \sin\left(\frac{\nu_n p_{i,n}}{\alpha_n}\right) + \left(m_{i,n} - \frac{m_i^{\max} + m_i^{\min}}{2}\right)\cos\left(\frac{\nu_n p_{i,n}}{\alpha_n}\right), \tag{20}$$

where $\alpha_n = \sqrt{(m_i^{\max} - m_{i,n})(m_{i,n} - m_i^{\min})}$.

The iteration process will be terminated if one of the following conditions occurs: (1) The misfit $\phi^d(\overline{\mathbf{m}}_n)$ is within a prescribed tolerance factor; (2) The difference between the misfit at two successive iterates n is within a prescribed tolerance factor; (3) the difference between the model parameters $\overline{\mathbf{m}}$ at two successive iterates n is within a prescribed tolerance factor; (4) The total number of iterations exceeds a prescribed maximum.

3. Numerical Example

As a test example we employ a model shown in Fig. 1(a). This model was originally used to study a CO_2 injection operation and is employed here as it includes smoothly varying dipping stratigraphy as well as sharp boundaries and deviated wells. The background model shown in Fig. 1(b) is obtained using single-well logs interpolated between the two wells. The hypothesized CO_2 injection region is shown in red in Fig. 1(a). The change between the true model and the background model is shown in Fig. 1(c) given in percentage difference (%). The data are collected using 41 transmitters and 41 receivers. The locations of the transmitters and receivers are denoted by 'T' and 'R' in Fig. 1. Thus we have 1681 complex-valued data points. After generating the synthetic data, we corrupted the data with random white noise that corresponds to 2% of the maximum amplitude of all data points. The inversion domain is from $x = -30$ m to $x = 350$ m and $z = 950$ m to $z = 1250$ m and is discretized into cells of dimensions 5 m by 5 m, hence the total number of unknown model parameters is 4636.

First we run our inversion algorithm using the L_2-norm regularizer given in (4) and (5). As the initial estimate we use the background model given in Fig. 1(b). Using this regularization term, the scheme took 15 iterations to converge. Figs. 1(d) and 1(e) show the percentage difference between the inverted resistivity and the background resistivity. The image obtained using the L_2-norm regularizer is shown in Fig. 1(d). The image obtained in this case has the appearance of a spatially smoothed version of the model changes in Fig. 1(c). Next we rerun our inversion code, however now we use the weighted L_2-norm regularization term given in (4) and (6). The inversion results after 19 iterations are shown in Fig. 1(e). By using the weighted L_2-norm regularizer we obtain a significant improvement in the reconstruction of the geometry and the amplitude of the change due to the CO_2 injection. Finally we note that one iteration of the scheme takes only 180 seconds on a PC with a Pentium IV 3.04 GHz processor.

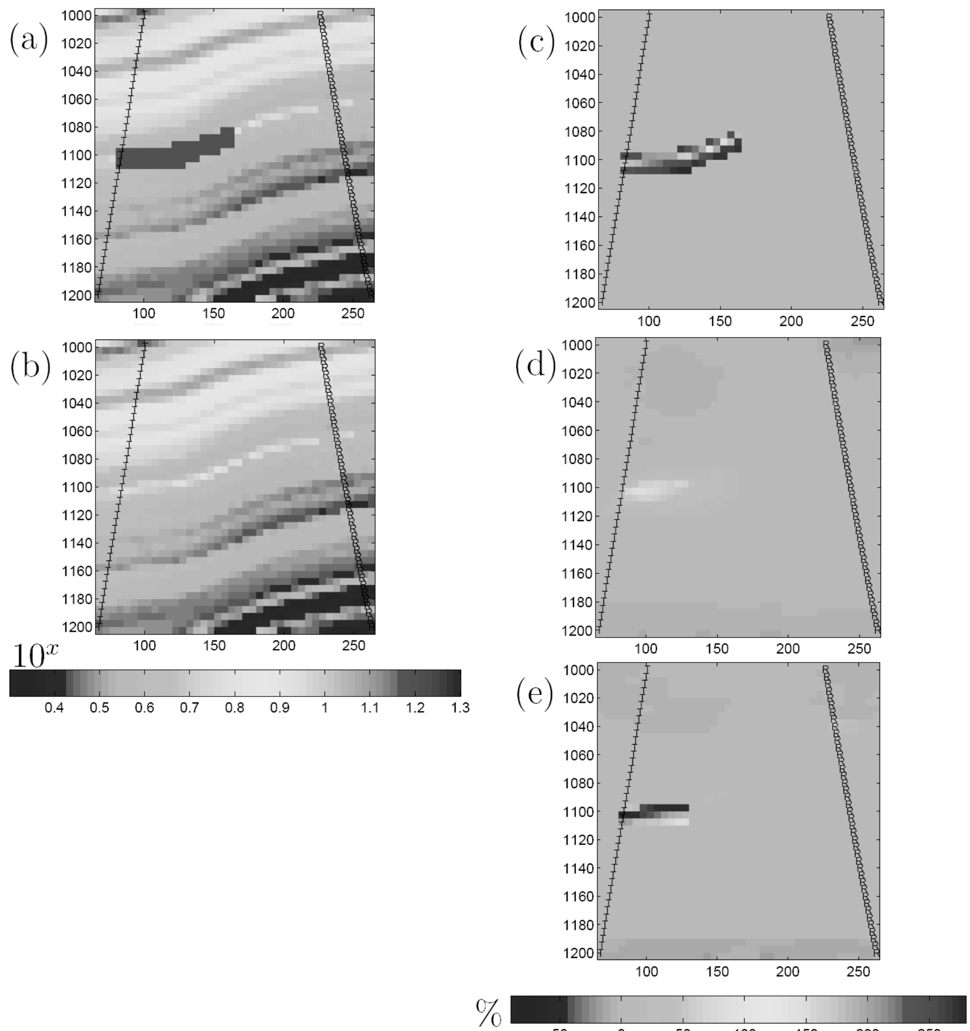

Figure 1: The resistivity distribution of the true model (a), of the initial model (b), the changes between (a) and (b) given in percentage (c), the inverted resistivity plotted as the change with respect to the model in (b) obtained using a L_2-norm regularizer (d) and a weighted L_2-norm regularizer (e).

REFERENCES

1. Dennis JR, J. E. and R. B. Schnabel, *Numerical Methods for Unconstrained Optimization and Nonlinear Equations*, Prentice Hall, Inc., New Jersey, 1983.
2. Habashy, T. M. and A. Abubakar, "A general framework for constraint minimization for the inversion of electromagnetic measurements," *Progress in Electromagnetic Research*, Vol. 46, 265–312, 2004.
3. Ingerman, D., V. L. Druskin, and L. Knizhnerman, "Optimal finite difference grids and rational approximations of the square root I. Elliptic problems," *Communications on Pure and Applied Mathematics*, LIII, 1039–1066, 2000.
4. Spies, B. R. and T. M. Habashy, "Sensitivity analysis of cross-well electromagnetics," *Geophysics*, Vol. 60, 834–845, 1995.
5. Van den Berg, P. M. and A. Abubakar, "Contrast source inversion method: state of art," *Progress in Electromagnetics Research*, Vol. 34, 189–218, 2001.
6. Wilt, M. J., D. L. Alumbaugh, H. F. Morrison, A. Becker, K. H. Lee, and M. Deszcz-Pan, "Crosshole electromagnetic tomography: system design considerations and field results," *Geophysics*, Vol. 60, 871–885, 1995.

A Rigorous 3-D MT Inversion

D. B. Avdeev[1,2] **and A. D. Avdeeva**[1]
[1]Dublin Institute for Advanced Studies, Ireland
[2]IZMIRAN, Russian Academy of Sciences, Russia

Abstract—The limited-memory quasi-Newton optimization method with simple bounds has been applied to develop a novel fully three-dimensional (3-D) magnetotelluric (MT) inversion technique. This nonlinear inversion is based on iterative minimization of a classical Tikhonov-type regularized penalty functional. But instead of the usual model space of log resistivities, the approach iterates in a model space with simple bounds imposed on the conductivities of the 3-D target. The method requires storage that is proportional to $n_{cp}\times N$, where the N is the number of conductivities to be recovered and n_{cp} is the number of the correction pairs (practically, only a few). This is much less than requirements imposed by other Newton type methods (that usually require storage proportional to $N\times M$, or $N\times N$, where M is the number of data to be inverted). Using an adjoint method to calculate the gradients of the misfit drastically accelerates the inversion. The inversion also involves all four entries of the MT impedance matrix. The integral equation forward modelling code *x3d* by Avdeev et al. ([1, 2]) is employed as an engine for this inversion. Convergence, performance and accuracy of the inversion are demonstrated on a 3D MT synthetic, but realistic, example.

1. Introduction

Limited memory quasi-Newton (QN) methods are becoming a popular tool for the numerical solution of three-dimensional (3-D) electromagnetic (EM) large-scale inverse problems ([11, 7]). The reason is that the methods require calculation of gradients of the misfit only, while at the same time avoiding calculations of second-derivative terms. They also require storing merely several pairs of so-called correction vectors that dramatically diminish the storage requirements. A more complete review on this subject may be found in [4].

In this paper we apply a limited memory QN optimization method with simple bounds (hereinafter, referred to as LMQNB) to solve the 3–D magnetotelluric (MT) inverse problem. In section 2 we briefly describe the setting of the inverse problem, as well as some key features of our implementation, referring the reader to the paper [3] for details.

In section 3, we develop the theory and basic equations for the calculation of gradients of the misfit. We demonstrate that the calculation of gradients at a given period is equivalent to only two forward modellings and does not depend on the number of conductivities to be recovered. The mathematical details of the approach are not presented here except the key formula (3), which is central to the method.

In section 4 we demonstrate how our inversion practically works on a synthetic, but realistic numerical example. This example includes a tilted conductive dyke in a uniform half-space (see [17]). The results presented are encouraging and suggest that the inversion may be successfully applied to solving realistic 3-D inverse problems with real MT data.

2. 3-D MT Inversion

Let us first consider a 3-D earth conductivity model discretized by N cells, such that $\sigma(\mathbf{r}) = \sum\limits_{k=1}^{N} \sigma_k \chi_k(\mathbf{r})$, where $\chi_k(\mathbf{r}) = \begin{cases} 1, \mathbf{r} \in V_k \\ 0, \mathbf{r} \notin V_k \end{cases}$, V_k is the volume occupied by k-th cell and $\mathbf{r} = (x, y, z)$. In the frame of MT inversion conductivities σ_k $(k = 1, \ldots, N)$ of the cells are sought. This is a typical optimization problem, such that $\varphi(\sigma, \lambda) \underset{\sigma,\lambda}{\rightarrow} \min$, with a penalty function φ given as

$$\varphi(\sigma, \lambda) = \varphi_d(\sigma) + \lambda\varphi_s(\sigma), \tag{1}$$

where $\varphi_d = \frac{1}{2}\sum\limits_{j=1}^{N_S}\sum\limits_{i=1}^{N_T} \alpha_{ji} tr[\overline{\mathbf{A}}_{ji}^T \mathbf{A}_{ji}]$ is the data misfit. Here $\sigma = (\sigma_1, \ldots, \sigma_N)^T$ is the vector consisting of the electrical conductivities of the cells; hereinafter superscript T means transpose and the upper bar stands for the complex conjugate; N is the number of the cells; N_S is the number of MT sites, $\mathbf{r}_j = (x_j, y_j, z = 0)$, where $j = 1, \ldots, N_S$; N_T is the number of the frequencies ω_i, where $i = 1, \ldots, N_T$; the 2×2 matrices $\mathbf{A}_{ji}$ are defined as

$\mathbf{A}_{ji} = \mathbf{Z}_{ji} - \mathbf{D}_{ji}$, where $\mathbf{Z}_{ji} = \begin{pmatrix} Z_{xx} & Z_{xy} \\ Z_{yx} & Z_{yy} \end{pmatrix}_{ji}$ and $\mathbf{D}_{ji} = \begin{pmatrix} D_{xx} & D_{xy} \\ D_{yx} & D_{yy} \end{pmatrix}_{ji}$ are matrices of the complex-valued predicted $\mathbf{Z}(\mathbf{r}_j, \omega_i)$ and observed $\mathbf{D}(\mathbf{r}_j, \omega_i)$ impedances, respectively; $\alpha_{ji} = \frac{2}{N_S N_T} \epsilon_{ji}^{-2} \left(tr[\overline{\mathbf{D}}_{ji}^T \mathbf{D}_{ji}] \right)^{-1}$ are the positive weights, where ϵ_{ji} is the relative error of the observed impedance $\mathbf{D}_{ji}$; and λ is a Lagrange multiplier. The sign $tr\,[\cdot]$ introduced above means the trace of its matrix argument, which is defined as $tr\,[\mathbf{B}] = B_{xx} + B_{yy}$, for any $\mathbf{B} = \begin{pmatrix} B_{xx} & B_{xy} \\ B_{yx} & B_{yy} \end{pmatrix}$. As prescribed by the Tikhonov regularization theory [15] the penalty function φ of (1) has a regularized part (a stabilizer) $\varphi_s(\sigma)$. This stabilizer can be chosen in different ways. However, this aspect of the problem is out of the scope of this paper. It is of importance that, as the conductivities $\sigma_k\,(k = 1, \ldots, N)$ must be non-negative and realistic, the optimization problem (1) is subject to the bounds

$$\mathbf{l} \leq \sigma \leq \mathbf{u}, \tag{2}$$

where $\mathbf{l} = (l_1, \ldots, l_N)^T$ and $\mathbf{u} = (u_1, \ldots, u_N)^T$ are respectively the lower and upper bounds and $l_k \geq 0\,(k = 1, \ldots, N)$.

Optimization method. We notice that problem (1)-(2) is a typically optimization problem with simple bounds (see [12]). To solve this problem we apply the limited memory quasi-Newton method with simple bounds. Our implementation of this method is described in a companion paper [3], which demonstrates the application of the method to the 1-D problem. At each iteration step l, we find the search direction $\mathbf{p}^{(l)}$ as $\mathbf{p}^{(l)} = -\mathbf{G}^{(l)}\mathbf{g}^{(l)}$, where $\mathbf{g}^{(l)} = (\frac{\partial \varphi}{\partial \sigma_1}, \ldots, \frac{\partial \varphi}{\partial \sigma_N})^T$ is the gradient vector and $\mathbf{G}^{(l)}$ is an approximation to the inverse Hessian matrix, that is updated at every iteration using the limited memory BFGS formula (see [12], formula (9.5), p.225). The next iterate $\sigma^{(l+1)}$ is then found as $\sigma^{(l+1)} = \sigma^{(l)} + \alpha^{(l)}\mathbf{p}^{(l)}$, where the step length $\alpha^{(l)}$ is computed by an inexact line search. What is crucial in this approach it is that it requires 1) relatively small storage proportional to $n_{cp} \times N$, where n_{cp} is the number of the correction pairs, and 2) only the calculation of gradients rather than the time-consuming sensitivities and/or the Hessian matrices.

Calculation of gradients. To derive derivatives $\frac{\partial \varphi_d}{\partial \sigma_k}$ we apply an adjoint method. This method uses the EM field reciprocity and has been applied previously to calculate the sensitivities ([16, 9]) and for forward modelling and inversion ([6, 13, 11, 5]). Let us now describe our implementation of such a technique.

It can be proven with some effort that

$$\frac{\partial \varphi_d}{\partial \sigma_k} = Re \left\{ \sum_{i=1}^{N_T} \int\limits_{V_k} tr\left[\mathbf{u}_i^T \mathbf{E}_i\right] dV \right\}, \tag{3}$$

where $tr[\mathbf{u}_i^T \mathbf{E}_i] = u_x^{(1)}E_x^{(1)} + u_y^{(1)}E_y^{(1)} + u_z^{(1)}E_z^{(1)} + u_x^{(2)}E_x^{(2)} + u_y^{(2)}E_y^{(2)} + u_z^{(2)}E_z^{(2)}$, the sign Re means the real part of its argument and the superscript 1 or 2 denotes polarization of the source $\mathbf{J}_i$. By definition, 3×2 matrices $\mathbf{E}_i(\mathbf{r}) = \begin{pmatrix} E_x^{(1)} & E_y^{(1)} & E_z^{(1)} \\ E_x^{(2)} & E_y^{(2)} & E_z^{(2)} \end{pmatrix}_i^T$ and $\mathbf{u}_i(\mathbf{r}) = \begin{pmatrix} u_x^{(1)} & u_y^{(1)} & u_z^{(1)} \\ u_x^{(2)} & u_y^{(2)} & u_z^{(2)} \end{pmatrix}_i^T$ satisfy the following equations

$$\nabla \times \nabla \times \mathbf{E}_i - \sqrt{-1}\omega_i \mu \sigma(\mathbf{r}) \mathbf{E}_i = \sqrt{-1}\omega_i \mu \mathbf{J}_i, \tag{4}$$

$$\nabla \times \nabla \times \mathbf{u}_i - \sqrt{-1}\omega_i \mu \sigma(\mathbf{r}) \mathbf{u}_i = \sqrt{-1}\omega_i \mu \left(\mathbf{j}_i^{ext} + \nabla \times \mathbf{h}_i^{ext} \right), \tag{5}$$

where $\mathbf{j}_i^{ext} = \sum_{j=1}^{N_S} \alpha_{ji} \mathbf{p}^T \overline{\mathbf{A}}_{ji} (\mathbf{H}_{ji}^{-1})^T \delta(\mathbf{r} - \mathbf{r}_j)$, $\mathbf{h}_i^{ext} = -\frac{1}{\sqrt{-1}\omega_i\mu} \sum_{j=1}^{N_S} \alpha_{ji} \mathbf{p}^T \mathbf{Z}_{ji}^T \overline{\mathbf{A}}_{ji} (\mathbf{H}_{ji}^{-1})^T \delta(\mathbf{r} - \mathbf{r}_j)$, μ is the magnetic permeability, δ is the Dirac's delta-function and $i = 1, \ldots, N_T$. Here $\mathbf{p} = \begin{pmatrix} 1 & 0 & 0 \\ 0 & 1 & 0 \end{pmatrix}$ is the projection matrix, 2×2 matrices $\mathbf{A}_{ji}$, $\mathbf{Z}_{ji}$ are previously explained and the 2×2 $\mathbf{H}_{ji} = \begin{pmatrix} H_x^{(1)} & H_y^{(1)} \\ H_x^{(2)} & H_y^{(2)} \end{pmatrix}_{ji}$ is composed of the magnetic fields calculated at the j-th MT site and at the i-th frequency. The key formula (3) practically means that computational loads for calculating gradient $(\frac{\partial \varphi}{\partial \sigma_1}, \ldots, \frac{\partial \varphi}{\partial \sigma_N})^T$ are equivalent to those for the solution of $2 \times N_T$ forward problems using Eq. (4) to find $\mathbf{E}_i$ and of $2 \times N_T$ adjoint problems using Eq. (5) to find $\mathbf{u}_i$ for all $i = 1, \ldots, N_T$. Straightforward calculation of the gradient would require solution of $2 \times N_T \times (N + 1)$ forward problems.

The approach described is quite general. It is not limited to magnetotellurics only, but can be applied to a variety of EM problems.

3. Model example

Let us demonstrate on a numerical example how MT inversion allows conductivity to be recovered. In Fig. 1 we present a model including a tilted 3 ohm-m dyke embedded into a 100 ohm-m half-space. The dyke is located at depth 200 to 700 m and it consists of 5 shifted adjacent blocks of $200\times800\times100\,\mathrm{m}^3$ size each. Our modeling domain comprises of $N_x \times N_y \times N_z$=16×24×8 rectangular prisms of $100\times100\times100\,\mathrm{m}^3$ size that cover the dyke and the some part of the surroundings. Notice that the volume lies at depths of 100–900 m.

The inversion domain coincides with the modeling domain. This means that $N = 3072$ conductivities σ_k $(k = 1, \ldots, N)$ of the prisms need to be recovered. The x3d forward modeling code described in ([1, 2]) was used as an engine for inversion to solve the forward and adjoint problems given in Eq. (4) and (5). It also was used to calculate 2×2 matrices $\mathbf{D}_{ji}$ of "observed" impedances at $N_T = 4$ frequencies of 1000, 100, 10 and 1 Hz. The impedances were computed at $N_S = 168$ sites r_j $(j = 1, \ldots, N_S)$ coinciding with the nodes of a homogeneous $n_x \times n_y$=12×14 grid, where 100 m is the distance between adjacent nodes.

In addition, the number of the correction pairs n_{cp} was chosen as 6, and the relative error ϵ_{ji} of the impedance was taken as 0.05. A 100 ohm-m uniform half-space was used as an initial guess. In Fig. 1 we also present the convergence of the inversion along with a set of 3-D models recovered at various iterations. It should be mentioned, however, that during inversion we did not use the stabilizer φ_s at all; the Lagrange multiplier λ was assigned a zero value. Instead, we assigned the lower conductivity limits of Eq. (2) as $l_k = 0.005$ $(k = 1, \ldots, N)$. In other words, resistivities $\rho_k = 1/\sigma_k$ of the cells were constrained from above by a value of 200 ohm-m. This turned out to play a similar role to that of regularization. It should be noted also that without putting

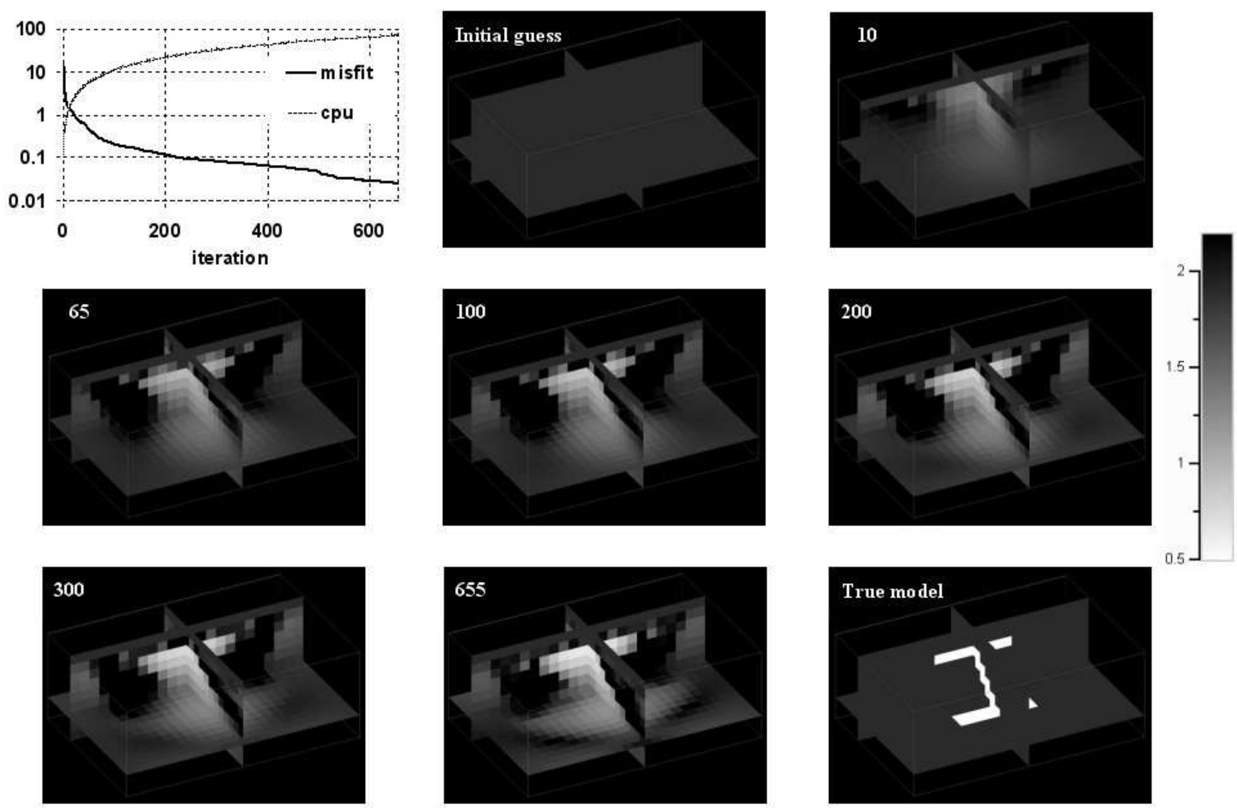

Figure 1: Convergence of the inversion for a 3-D model of a 3 ohm-m dyke in a uniform 100 ohm-m half-space. The left-upper panel presents the misfit and cpu time vs the iteration number. Other panels present images of the initial guess, the true model, as well as the models obtained at various stages of inversion. Number of iterations is given in upper-left corner of each panel.

constraints on l_k the iteration method without a stabilizer (i. e., when $\lambda = 0$) stagnates, when the misfit φ_d

drops to a value of 1.3 and it fails to produce a good conductivity image (not presented here).

4. Conclusion

In this paper we have developed a novel approach to 3-D MT inversion. The most essential part of our derivation is that we developed and implemented the adjoint method to derive explicit expressions for the calculation of the gradients of the misfit. Our development is quite general and is not limited to magnetotellurics alone. It can be applied to a variety of EM problems, such as marine controlled-source EM etc. With a synthetic MT example, we have obtained the first promising results of convergence of our solution. The method still needs further development to become a user-end product of universal value to the EM community.

Further work will be concentrated on adapting various types of regularization techniques, and introducing the static shift into the penalty function (1). It is also planned to apply our inversion scheme to an experimental data set. However, previous examples from other 3-D MT inversion software developers (see [8, 10, 14, 17]) indicate that successful verification of the inversion technique even on a single practical dataset is a complex task and may take some time.

Acknowledgment

This work was supported by the Cosmogrid project, which is funded by the Programme for Research in Third Level Institutions under the National Development Plan and with assistance from the European Regional Development Fund. Thanks to Brian O'Reilly for corrections to English. We acknowledge an anonymous reviewer for a very encouraging opinion on the results of our study. AA also acknowledges the constructive support of her supervisors Alan Jones and Colin Brown.

REFERENCES

1. Avdeev, D. B., A. V. Kuvshinov, O. V. Pankratov, and G. A. Newman, "High-performance three-dimensional electromagnetic modeling using modified neumann series. Wide-band numerical solution and examples," *J. Geomagn. Geoelectr.*, Vol. 49, 1519–1539, 1997.
2. Avdeev, D. B., A. V. Kuvshinov, O. V. Pankratov, and G. A. Newman, "Three-dimensional induction logging problems, Part I, An integral equation solution and model comparisons," *Geophysics*, Vol. 67, 413–426, 2002.
3. Avdeeva, A. D. and D. B. Avdeev, "QN inversion of large-scale MT data," *this volume*.
4. Avdeev, D. B., "Three-dimensional electromagnetic modelling and inversion from theory to application," *Surveys in Geophysics*, Vol. 26, 767–799, 2005.
5. Chen, J., D. W. Oldenburg, and E. Haber, "Reciprocity in electromagnetics: application to modeling marine magnetometric resistivity data," *Phys. Earth Planet. Inter.*, Vol. 150, 45–61, 2005.
6. Dorn, O., H. Bertete-Aguirre, J. G. Berryman, and G. C. Papanicolaou, "A nonlinear inversion method for 3D electromagnetic imaging using adjoint fields," *Inverse Problems* , Vol. 15, 1523–1558, 1999.
7. Haber, E., "Quasi-Newton methods for large-scale electromagnetic inverse problems," *Inverse problems*, Vol. 21, 305–323, 2005.
8. Mackie, R. L., W. Rodi, and M. D. Watts, "3-D magnetotelluric inversion for resource exploration," *71st Annual Internat. Mtg. Extended Abstracts, SEG*, 1501–1504, 2001.
9. McGillivray, P. R. and D. W. Oldenburg, "Methods for calculating Frechet derivatives and sensitivities for the non-linear inverse problems," *Geophysics*, Vol. 60, 899–911, 1990.
10. Newman, G. A., S. Recher, B. Tezkan, and F. M. Neubauer, "3D inversion of a scalar radio magnetotelluric field data set," *Geophysics*, Vol. 68, 791–802, 2003.
11. Newman, G. A. and P. T. Boggs, "Solution accelerators for large-scale three-dimensional electromagnetic inverse problem," *Inverse Problems*, Vol. 20, s151–s170, 2004.
12. Nocedal, J. and S. J. Wright, *Numerical optimization*, Springer, 1999.
13. Rodi, W. and R. L. Mackie, "Nonlinear conjugate gradients algorithm for 2-D magnetotelluric inversion," *Geophysics*, Vol. 66, 174–187, 2001.
14. Siripunvaraporn, W., M. Uyeshima, and G. Egbert, "Three-dimensional inversion for network-magnetotelluric data," *Earth Planets Space*, Vol. 56, 893–902, 2004.
15. Tikhonov, A. N. and V. Y. Arsenin, *Solutions of ill-posed problems*, Wiley, New York, 1977.
16. Weidelt, P., "Inversion of two-dimensional conductivity structures," *Physics of the Earth and Planetary Interiors*, Vol. 10, 281-291, 1975.
17. Zhdanov, M. S. and E. Tolstaya, "Minimum support nonlinear parametrization in the solution of a 3D magnetotelluric inverse problem," *Inverse problems*, Vol. 20, 937–952, 2004.

Contrast Source Inversion of 3D Electromagnetic Data

P. M. van den Berg
Delft University of Technology, The Netherlands

A. Abubakar and T. M. Habashy
Schlumberger-Doll Research, USA

Abstract—This paper discusses the full vector three-dimensional inverse electromagnetic scattering problem. We consider the determination of the location and the electromagnetic composition of an inhomogeneous bounded object in a homogeneous embedding from measurements of the scattered electromagnetic wavefield, when the object is illuminated by a known single frequency wavefield. To solve this large-scale nonlinear inversion problem, we apply the so-called multiplicative regularized contrast source method.

1. Introduction

In this MR-CSI method we reconstruct the complex permittivity contrast and the so-called contrast sources (the product of the contrast and the fields) by minimizing a cost functional in which the residual errors in the field equations occur. This minimization is carried out in an alternating way. In each iterative step we update the contrast and the contrast sources each using one conjugate gradient step so that the total computational complexity of the method is equal to the complexity of solving only two forward problems. By operating in this manner solving a full three-dimensional vector nonlinear inverse scattering problem is feasible. Further this method is equipped with total variation type regularization. This regularization is included as a multiplicative constraint, so that the regularization parameter needed in the minimization process is determined automatically. The multiplicative type of regularization handles noisy as well as limited data in a robust way without the usually necessary a *priori* information. We illustrate the performance by presenting some inversion results from 3D electromagnetic experimental data. Further, we discuss an inversion method to invert not only the complex electric contrast but also the magnetic contrast of a three-dimensional object. The contrast source inversion is extended by introducing both the electric contrast sources and the magnetic contrast sources. Further, an extended cost functional is introduced in which the residual errors in both the electric and magnetic field equations occur. Additionally, the multiplicative regularization is extended such that the spatial variations of both the electric and magnetic contrast are minimized. Since in [1] we tested the algorithm for a heterogeneous object that has intermingled electric and magnetic contrast, we will present a numerical example with disjoint electric and magnetic contrast.

2. Inversion Algorithm

The Multiplicative Regularized Born Inversion (MRCSI) consists of an algorithm to construct sequences $w_j = \{w_{j,n}\}$ and $\chi = \{\chi_n\}$ which iteratively reduce the value of the cost functional,

$$F_n = [F_S + F_{D,n}]F_n^R = \left[\frac{\sum_j \|u_j^{\mathrm{sct}} - G_S w_j\|_S^2}{\sum_j \|u_j^{\mathrm{sct}}\|_S^2} + \frac{\sum_j \|\chi u_j^{\mathrm{inc}} - w_j + G_D w_j\|_D^2}{\sum_j \|\chi_{n-1} u_j^{\mathrm{inc}}\|_D^2}\right] \frac{1}{V} \int\limits_D \frac{|\nabla\chi|^2 + \delta_n^2}{|\nabla\chi_{n-1}|^2 + \delta_n^2} dv$$

where
$[G_S w_j](\bar{x}) = \int\limits_D g(\bar{x}, \bar{x}')w_j(\bar{x}')dv(\bar{x}')$, $\bar{x} \in S$, and $[G_D w_j](\bar{x}) = \int\limits_D g(\bar{x}, \bar{x}')w_j(\bar{x}')dv(\bar{x}')$, $\bar{x} \in D$. The subscripts D and S indicate that the observation point $\bar{x}$ lies either in D, a bounded domain containing the scattering object, or S, a domain disjoint from D on which the scattered field u_j^{sct}, $j = 1, \ldots, J$, is measured for each known incident field u_j^{inc}. The symbol V denotes the volume of the domain D. Further, $\| \bullet \|_S$ and $\| \bullet \|_D$ denote the norms on $L_2(S)$ and $L_2(D)$. Further, g denotes the Green function of the background medium, while χ denotes the contrast with the background medium. For the steering parameter δ_n^2 we choose progressively decreasing values in such a way that, for given contrast sources, the cost functional F_n as a function of the contrast χ, remains convex during all iterations. We relate this parameter directly to the decreasing object error $F_{D;n-1}$. The structure of the cost functional is such that it will minimize the regularization factor F_n^R with a large weighting parameter in the beginning of the optimization process, because the value of $F_S + F_{D;n-1}$ is still large, and that it will gradually minimize more and more the error in the data and object equations when the value of F_n^R has reached a nearly constant value equal to one. If noise is present in the data, the data error term F_S will remain at a large value during the optimization and therefore, the weight of the regularization factor will be more significant. Hence, the hindering character of noise will, at all times, be suppressed in the reconstruction

process, but at the cost of decreased resolution. This minimization is carried out in two alternate steps. For given contrast, χ_{n-1}, the contrast sources are updated via conjugate gradient directions of the cost functional, while for given contrast sources, $w_{j,n}$, the contrast is updated via a preconditioned conjugate gradient direction of the cost functional.

3. Integral Operators for Electric Contrast

Firstly we consider the 3D electromagnetic inversion problem, where the scattering object only has electric contrast χ^E with respect to its embedding. Then we deal with electric contrast sources

$$\bar{w}_j^E(\bar{x}) = \chi^E(\bar{x})\bar{E}(\bar{x}), \quad \text{where} \quad \chi^E(\bar{x}) = \frac{\sigma'(\bar{x})}{\sigma'_b} - 1,$$

with complex conductivity, $\sigma'(\bar{x}) = \sigma(\bar{x}) - i\omega\varepsilon(\bar{x})$, for the inhomogeneous object, and the complex conductivity, $\sigma'_b = \sigma_b - i\omega\varepsilon_b$, for the homogeneous embedding. The scalar Green function is given by

$$g(\bar{x}, \bar{x}') = \frac{\exp(ik_b|\bar{x} - \bar{x}'|}{4\pi|\bar{x} - \bar{x}'|}, \quad k_b = \sqrt{(i\omega\mu_b\sigma'_b)}.$$

In this 3D case the field function u_j^{inc} to be replaced by the incident electric field vector $\bar{E}_j^{\text{inc}}$ and the scattered field data u_j^{sct} has to be replaced by either the measured scattered electric field vector $\bar{E}_j^{\text{sct}}$ for an electric dipole receiver or the measured scattered magnetic field vector $\bar{H}_j^{\text{sct}}$ for a magnetic dipole receiver. The governing integral operators become

$$G_S w_j := \begin{cases} [k_b^2 + \nabla\nabla\bullet]\bar{A}_j^E & \text{for an electric dipole receiver,} \\ \sigma'_b\nabla \times \bar{A}_j^E & \text{for a magnetic dipole receiver,} \end{cases}$$

and

$$G_D w_j := [k_b^2 + \nabla\nabla\bullet]\bar{A}_j^E, \qquad \text{where } \bar{A}_j^E(\bar{x}) = \int_D g(\bar{x}, \bar{x}')\bar{w}_j^E(\bar{x}')dv(\bar{x}').$$

We will illustrate the performance of this type of inversion scheme by presenting some inversion results from 3D electromagnetic experimental data.

4. Integral Operators for Electric and Magnetic Contrast

Secondly, we consider the 3D electromagnetic inversion problem. where the scattering object has both electric contrast χ^E and magnetic contrast χ^H with respect to its embedding. In addition the electric contrast sources, we also deal with the magnetic contrast sources

$$\bar{w}_j^H(\bar{x}) = \chi^H(\bar{x})\bar{H}(\bar{x}), \quad \text{where} \quad \chi^H(\bar{x}) = \frac{\mu(\bar{x})}{\mu_b} - 1,$$

with permeability, $\mu(\bar{x})$, for the inhomogeneous object, and permeability, μ_b, for the homogeneous embedding. In this 3D case the cost functional has to be extended to the following form

$$\begin{aligned} F_n \;=\; & [F_S^E(\bar{w}_j^E, \bar{w}_j^H) + F_{D,n}^E(\bar{w}_j^E, \bar{w}_j^H, \chi^E)]\frac{1}{V}\int_D \frac{|\nabla\chi^E|^2 + (\delta_n^E)^2}{|\nabla\chi_{n-1}^E|^2 + (\delta_n^E)^2}dv \\ & +[F_S^H(\bar{w}_j^E, \bar{w}_j^H) + F_{D,n}^H(\bar{w}_j^E, \bar{w}_j^H, \chi^H)]\frac{1}{V}\int_D \frac{|\nabla\chi^H|^2 + (\delta_n^H)^2}{|\nabla\chi_{n-1}^H|^2 + (\delta_n^H)^2}dv \end{aligned}$$

where

$$F_S^E(\bar{w}_j^E, \bar{w}_j^H) = \frac{\sum_j \|\bar{E}_j^{\text{sct}} - G_S^E(\bar{w}_j^E, \bar{w}_j^H)\|_S^2}{\sum_j \|\bar{E}_j^{\text{sct}}\|_S^2} \quad \text{for an electric dipole receiver,}$$

$$F_S^H(\bar{w}_j^E, \bar{w}_j^H) = \frac{\sum_j \|\bar{H}_j^{\text{sct}} - G_S^H(\bar{w}_j^E, \bar{w}_j^H)\|_S^2}{\sum_j \|\bar{H}_j^{\text{sct}}\|_S^2} \quad \text{for a magnetic dipole receiver,}$$

and

$$F_{D,n}^E(\bar{w}_j^E, \bar{w}_j^H, \chi^E) = \frac{\sum_j \|\chi^E\bar{E}_j^{\text{inc}} - \bar{w}_j^E + G_D^E(\bar{w}_j^E, \bar{w}_j^H)\|_D^2}{\sum_j \|\chi_{n-1}^E\bar{E}_j^{\text{inc}}\|_D^2},$$

$$F_{D,n}^H(\bar{w}_j^E, \bar{w}_j^H, \chi^H) = \frac{\sum_j \|\chi^H\bar{H}_j^{\text{inc}} - \bar{w}_j^H + G_D^H(\bar{w}_j^E, \bar{w}_j^H)\|_D^2}{\sum_j \|\chi_{n-1}^H\bar{H}_j^{\text{inc}}\|_D^2},$$

The governing integral operators become

$$G_S^E(\bar{w}_j^E, \bar{w}_j^H) = [k_b^2 + \nabla\nabla\bullet]\bar{A}^E + i\omega\mu_b \nabla \times \bar{A}^H, \quad G_S^H(\bar{w}_j^E, \bar{w}_j^H) = \sigma_b' \nabla \times \bar{A}^E + [k_b^2 + \nabla\nabla\bullet]\bar{A}^H,$$

for observation points in the data domain S,

and

$$G_D^E(\bar{w}_j^E, \bar{w}_j^H) = [k_b^2 + \nabla\nabla\bullet]\bar{A}^E + i\omega\mu_b \nabla \times \bar{A}^H, \quad G_D^H(\bar{w}_j^E, \bar{w}_j^H) = \sigma_b' \nabla \times \bar{A}^E + [k_b^2 + \nabla\nabla\bullet]\bar{A}^H,$$

for observation points in the data domain D,

where

$$\bar{A}^E(\bar{x}) = \int_D g(\bar{x}, \bar{x}')\bar{w}_j^E(\bar{x}')dv(\bar{x}') \quad \text{and} \quad \bar{A}^H(\bar{x}) = \int_D g(\bar{x}, \bar{x}')\bar{w}_j^H(\bar{x}')dv(\bar{x}')$$

The minimization of the extended cost functional is carried out iteratively in three alternate steps:

- For given electric contrast χ_{n-1}^E and magnetic contrast χ_{n-1}^H, the contrast source vector $\{\bar{w}_j^E, \bar{w}_j^H\}$ is updated via conjugate gradient directions of the cost functional.
- For given electric contrast sources $\bar{w}_{j,n}^E$ and magnetic contrast sources $\bar{w}_{j,n}^H$, the electric contrast χ^E is updated via preconditioned conjugate directions.
- For given electric contrast sources $\bar{w}_{j,n}^E$ and magnetic contrast sources $\bar{w}_{j,n}^H$, the magnetic contrast χ^H is updated via preconditioned conjugate directions.

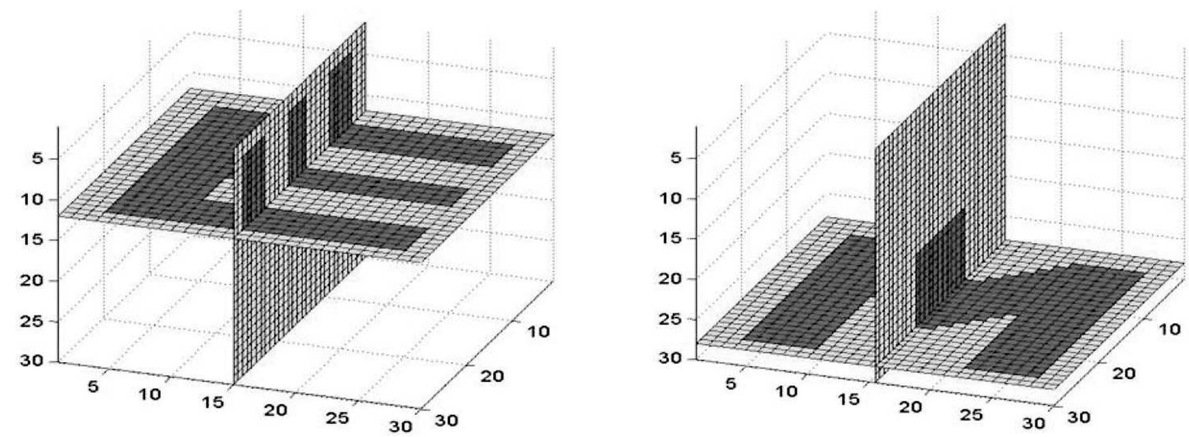

Figure 1: 3D scattering object in a $3\lambda \times 3\lambda \times 3\lambda$ vacuum domain with disjoint electric and magnetic contrast.

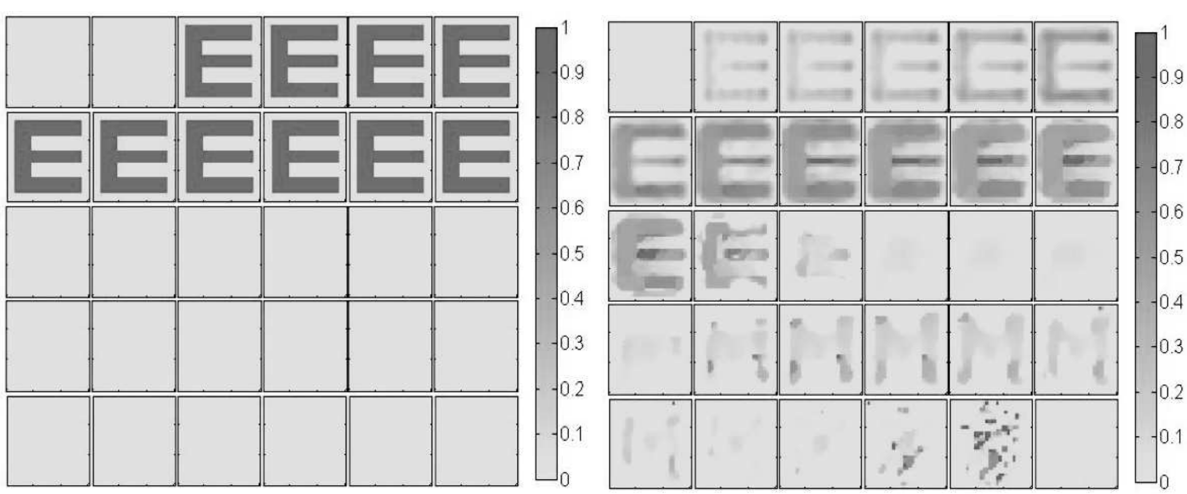

Figure 2: Exact (left) and reconstructed (right) of the real part of the electric contrast, at 30 different horizontal planes.

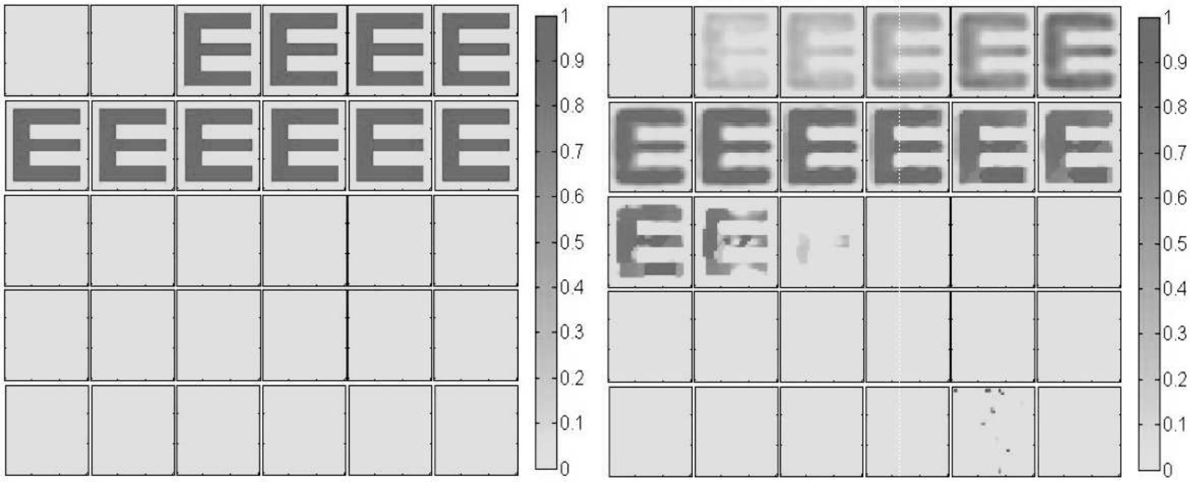

Figure 3: Exact (left) and reconstructed (right) of the imaginary part of the electric contrast, at 30 different horizontal planes.

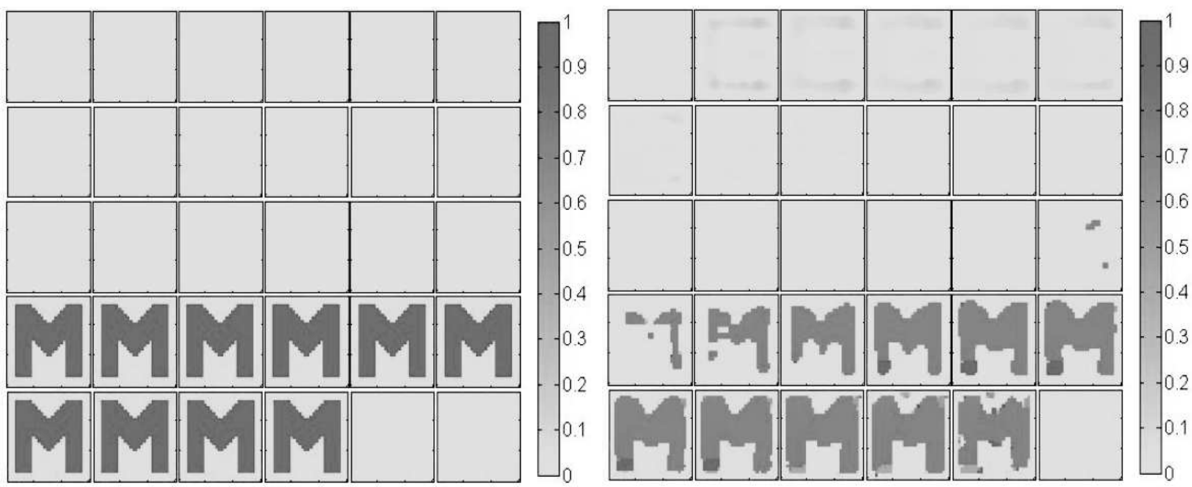

Figure 4: Exact (left) and reconstructed (right) magnetic contrast, at 30 different horizontal planes.

As numerical example we have simulated electromagnetic field data from an object in a vacuum domain with size of $3\lambda \times 3\lambda \times 3\lambda$. One part of the object is "E"-shaped and has only electric contrast given by the complex contrast function $\chi^E = 1 + 1i$, while the other part is "M"-shaped and has only magnetic contrast given by the real contrast function $\chi^H = 1$ (see Figure 1). We use vertical magnetic dipoles both as transmitters and as receivers. In an area above the domain under investigation, 30 transmitters have been located, viz., at the vertical position $x_3 = -0.1\lambda$ In an area below the domain under investigation, 30 receivers have been located, viz., at the vertical position $x_3 = 3.1\lambda$. Hence, we have only 900 complex-valued data points. The square domain D under investigation is subdivided into $30 \times 30 \times 30$. This means that we have 27000 unknown complex-valued electric contrast points plus 27000 unknown real-valued magnetic contrast points. The reconstruction results are given in Figures 2–4. Although the number of unknowns is much larger than the number of known data points, we observe a very good reconstruction in the horizontal plane through the middle of the "E"-shaped object (see Figure 3) and the middle of the "M"-shaped object (see Figure 4), while the reconstruction deteriorates towards the top and bottom part the objects.

We conclude that the present extended form of the MR-CSI method enables the full nonlinear 3D inversion of large scale electromagnetic data.

REFERENCES

1. Abubakar and P. M. van den Berg, "Iterative forward and inverse algorithms based on domain integral equations for three-dimensional electric and magnetic objects," *Journal of Computational Physics*, Vol. 195, 236–262, 2004.